

Origin of the Unusual Temperature Dependence of the Upper Critical Field of Kagome Superconductor CsV₃Sb₅: Multiple Bands or van Hove Singularities?

Ramakanta Chapai,^{1,*} A. E. Koshelev,^{2,†} M. P. Smylie,^{1,3} D. Y. Chung,¹ Asghar Kayani,⁴ Khushi Bhatt,⁵ Gaurab Rimal,⁴ M. G. Kanatzidis,^{1,6} W.-K. Kwok,¹ J. F. Mitchell,¹ and Ulrich Welp^{1,‡}

¹*Materials Science Division, Argonne National Laboratory, Lemont, IL 60439, USA*

²*Department of Physics and Astronomy, University of Notre Dame, Notre Dame, IN 46656, USA*

³*Department of Physics and Astronomy, Hofstra University, Hempstead, NY 11549, USA*

⁴*Department of Physics, Western Michigan University, Kalamazoo, MI 49008, USA*

⁵*Physics Division, Argonne National Laboratory, Lemont, IL 60439, USA*

⁶*Department of Chemistry, Northwestern University, Evanston, IL 60201, USA*

Van Hove singularities (vHs) located close to the Fermi level in Kagome superconductors AV₃Sb₅ (A = K, Rb, Cs) have profound influence on their electronic and transport characteristics. Specifically, magneto-transport and susceptibility measurements on CsV₃Sb₅ reveal an anomalous temperature dependence of the upper critical field $H_{c2}(T)$, characterized by a pronounced upward curvature for both in-plane and c -axis magnetic fields, with zero-temperature H_{c2} values of ~ 6.0 T and ~ 1.2 T, respectively. Our theoretical analysis, using a newly developed single-band model incorporating vHs and gap anisotropy, suggests that the observed upper critical field behavior is predominantly driven by the anisotropy of the Fermi velocity originating from vHs, instead of multi-band effects or gap anisotropy. Increased electron scattering introduced by proton irradiation defects smears out the vHs, reduces anisotropy, and recovers the conventional $H_{c2}(T)$ behavior, corroborating our proposed model.

The appearance of van Hove singularities (vHs), Dirac cones, flat bands, and geometrical frustration are hallmarks of Kagome lattices, making this structural motif a fruitful platform for the exploration of frustrated magnetism, spin liquid states, electronic correlations, non-trivial band topology, anomalous Hall effect and various types of charge order [1-6]. Accordingly, the recent discovery of superconductivity ($T_c \sim 0.9-3$ K) and its complex interplay with charge density wave (CDW) order ($T_{CDW} \sim 78-104$ K) in the metallic Kagome lattice compounds AV_3Sb_5 ($A = K, Rb,$ and Cs) has generated substantial interest in this class of materials [7-17]. A distinctive characteristic of these compounds is the proximity of the Fermi energy to vHs, as revealed by density functional theory (DFT) calculations [8, 18-23], and as observed in angle-resolved photoemission spectroscopy (ARPES) [8, 21, 22, 24-26]. This proximity is a possible contributor driving the CDW transition [27-30]; it also induces enhanced electronic density of states in specific regions of the Fermi surface, accompanied by a high degree of *anisotropy* in the Fermi velocity. Such anisotropy manifests in macroscopic properties of AV_3Sb_5 . Indeed, we have recently shown [31] that the unconventional magneto-transport properties of CsV_3Sb_5 can be explained by considering the anisotropic Fermi surface structure. Other quantities that are expected to reflect this anisotropy of the Fermi velocity include the superconducting penetration depth and the upper critical field, H_{c2} [32]. However, disentangling the effects of Fermi surface anisotropy, multiple bands, and possible gap anisotropy on the superconducting properties has proven to be challenging [33].

In this letter, we present a combined experimental and theoretical study of the upper critical field of CsV_3Sb_5 and its anisotropy. Our purpose is to link the superconducting phase boundary, $H_{c2}(T)$, to the Fermi surface structure, and to the question of multiband superconductivity in this Kagome metal [5, 13, 16, 34-40]. Measurements of $H_{c2}(T)$ in single crystal CsV_3Sb_5 reveal a pronounced upward curvature for c -axis as well as ab -plane magnetic fields. By incorporating experimental data with theoretical modeling, we demonstrate that the observed upward curvature is driven by anisotropy of the Fermi velocity, rather than multiband effects or gap anisotropy. In our theoretical framework, anisotropy of the Fermi velocity is induced by the proximity to vHs, and the formalism is general, capable of accommodating other sources of anisotropy. We test this model via proton irradiation to induce defects that are expected to suppress the anisotropy. Indeed, with increased proton dosing, the upwards curvature observed in $H_{c2}(T)$ in the pristine sample is

progressively suppressed, ultimately recovering the conventional Maki-de Gennes dirty-limit [41-43] behavior expected of a single, isotropic gap, corroborating our model.

High-quality single crystals of CsV_3Sb_5 were grown and characterized as described in our earlier works [31, 44-46]. Electrical resistivity measurements were performed in a 9-1-1 T triple-axis vector magnet inside a dilution refrigerator (Bluefors LD400) using the standard four-probe method with current applied along the ab -plane. The pristine crystals display superconducting and CDW transitions near $T_c \sim 3.5$ K and $T_{\text{CDW}} \sim 94$ K, respectively, as shown in the Supplemental Materials Fig. S1 (a-b) [44]. Irradiation of the samples with 5-MeV protons was performed at the tandem van de Graaff accelerator at Western Michigan University [44, 47].

The upper critical field $H_{c2}(T)$ is deduced from the measurement of the temperature dependence of the electrical resistivity $\rho(T)$ in various fields applied along the c -axis and the ab -plane as presented in Figs. 1(a) and 1(b), respectively for the pristine CsV_3Sb_5 . Upon the application of a field, the superconducting transition shifts in an almost parallel fashion to lower temperatures; in high fields, it undergoes slight broadening. In the normal state, there is a noticeable magnetoresistance (MR) for $H \parallel c$, while the MR is significantly smaller for $H \parallel ab$. Such behavior is expected in a model of semi-classical magnetoresistance for an anisotropic layered material [48, 49]. From the data in Figs. 1(a-b), we construct the temperature-field superconducting phase diagram of pristine CsV_3Sb_5 (crystal S1), shown in Fig. 1(c), for both field orientations; we define T_c as the midpoint of the transitions. The superconducting transitions display some structure, a feature frequently seen on CsV_3Sb_5 crystals [8-10, 50-52]. Measurements on a second crystal yield identical results (shown in Fig. S2 [44]), indicating that the observed behavior is intrinsic; specifically, for both orientations, the $H_{c2}(T)$ phase boundary displays pronounced upwards curvature, see Fig. 1(c, d). This behavior cannot be accounted for in the standard Werthamer-Helfand-Hohenberg (WHH) description [41] and is often interpreted as a characteristic feature of superconductors possessing multiple gaps [13, 16, 35, 53-56] or an anisotropic gap [33, 57-59]. While Fig. 1(d) shows as-measured H_{c2} -data, in Fig. 1(c) data normalized to the Ginzburg-Landau (GL) upper critical fields $H_{c2,\alpha}^{GL} = -dH_{c2,\alpha}/dT|_{T_c} T_c$ are presented, highlighting that the upward curvature is more pronounced for the c -axis.

The resulting superconducting anisotropy, $\Gamma = H_{c2}^{ab}/H_{c2}^c$ exhibits a strong temperature dependence (see Fig. 2(d)). While a sizable superconducting anisotropy might be expected given the layered crystal structure, the clear decrease in $\Gamma(T)$ with decreasing temperature (≈ 8.5 near

T_c to ≈ 5.5 at low temperatures) is not expected in the conventional single-band description. It is, however, another signature of either multi-gap or anisotropic gap superconductivity [33, 57-66]. In particular, the decrease in anisotropy with decreasing temperature is similar to that observed in FeAs-based superconductors [67] but opposite to that found for the archetypal multi-gap MgB₂ [55, 68]. For a two-band superconductor, such temperature variation of the H_{c2} anisotropy may arise when the band with the larger weight has a much smaller in-plane Fermi velocity and is less anisotropic [32].

Kagome AV₃Sb₅ superconductors have a rather complicated electronic band structure [7], and a complete first-principles calculation of the upper critical field is currently not feasible. Therefore, we employ simplified models capable of providing insight into the data. As it is common to attribute a pronounced upward curvature of $H_{c2}(T)$ such as shown in Fig. 1(c, d) to multiple-band effects, we first explore a two-band model to describe our data. Our model assumes two open Fermi surface sheets in the form of warped cylinders, reminiscent of the Sb-derived sheet centered on the Γ -A line [20]. Each Fermi surface is characterized by a superconducting gap Δ_α , and an in-plane Fermi velocity, v_α , each assumed to be isotropic in the plane. Following previous work [32, 66], we can present the equation for the upper critical field in the following form [44]

$$-\ln t = \sum_\alpha w_\alpha \int_0^\infty \frac{t ds}{\sinh(ts)} \left[1 - \left\langle \exp \left(-\frac{\hbar^2 v_\alpha^2 H}{8\pi k_B^2 T_c^2 \Phi_0} s^2 \right) \right\rangle_\alpha \right] \quad (1)$$

This relation is based on the quasi-classical Eilenberger equations applicable to clean superconductors; paramagnetic limiting is not included. Here, $t \equiv T/T_c$ is the reduced temperature, w_α are the band weights defined as $w_\alpha = n_\alpha \Delta_\alpha^2 / \sum_\beta n_\beta \Delta_\beta^2$ and satisfying $\sum_\alpha w_\alpha = 1$ with the fractional density of states $n_\alpha = N_\alpha / \sum_\beta N_\beta$. For the case of a two-band system, one finds $w_1 = 1/(1 + r_n r_\Delta)$ and $w_2 = r_n r_\Delta / (1 + r_n r_\Delta)$, where $r_n = N_2/N_1$ and $r_\Delta = \Delta_2^2/\Delta_1^2$ are the ratios of the band density of states and of the squared gaps. In Eq. (1), $\langle \dots \rangle_\alpha$ notates averaging over the α Fermi surface sheet, H is the applied field, k_B is the Boltzmann constant and Φ_0 the flux quantum. In this model, the shape of $H_{c2}(T)$ is determined by *four* reduced parameters: the band weight w_1 , the ratio of squares of in-plane Fermi velocities $r_v = v_{F2}^2/v_{F1}^2$, and two reduced hopping integrals: t_{z1}/ε_{F1} and t_{z2}/ε_{F2} [44]. In general, $H_{c2}(T)$ acquires an upward curvature when a band with larger weight has smaller Fermi velocity.

The simultaneous fitting of the in-plane and c -axis $H_{c2}(T)$ data yields curves that describe the data well, as shown in Fig. 1(c) with the fitting parameters included in the figure. This analysis

yields zero-temperature H_{c2} values of ~ 1.2 T (c -axis) and ~ 6.0 T (ab -plane). We note, however, that the fit depends on the product $r_v r_\Delta$ such that neither the gap ratio nor the individual gaps can be independently determined. A remarkable feature of the experimental results is the large enhancement of H_{c2} over the GL value by more than a factor of two for the c -axis while the standard WHH model would predict a reduction to $\sim 0.71 H_{c2}^{GL}$. In the quasi-2D limit, that is, small c -axis hopping integrals, the zero-temperature enhancement resulting from our model can be expressed in closed form as [44]: $H_{c2}(0)/H_{c2}^{GL} = 0.59 r_v^{w_1} [w_1/r_v + (1 - w_1)] \approx 2.1$. The key fit parameter required for this property is the large value of r_v ($= 57.6$).

Using the extremal cross sections of the Sb-derived Fermi surface sheet as predicted in DFT calculations [20], one finds a c -axis hopping integral of $t_z/E_F \sim 0.12$ for this sheet which is remarkably close to the fitted value of 0.133 for the ‘second’ band. Then, in this assignment, it is the ‘first’ band that has a much smaller Fermi velocity resulting in the large ratio $r_v = 57.6$. The actual physical realization of the ‘first’ band is not specified in this model and the hopping integral t_z/E_F should be regarded merely as a quantification of c -axis dispersion. Nevertheless, in light of the small Fermi velocity, it is tempting to relate the ‘first’ band to the large hexagonal Fermi surface sheet in close proximity to the vHs [31].

It has previously been noted [33] that the signatures of two gaps and of strongly anisotropic single bands in quantities such as the superconducting specific heat, the upper critical field and the superfluid density are very similar and difficult to distinguish experimentally. In particular, the presence of vHs in the electronic spectrum of Kagome superconductors causes strong anisotropy of the Fermi velocity which naturally leads to a pronounced upward curvature of $H_{c2}(T)$, as demonstrated previously in the 2D case [69-71]. We therefore consider a single-band model in which the Fermi level is positioned close to the van Hove singularities and re-write Eq. (1) for a single band with a wavevector dependent Fermi velocity as given by the hyperbolic sections of the Fermi surface [31, 41, 44, 66]

$$-\ln t = \int_0^\infty \frac{t ds}{\sinh(ts)} \left\{ 1 - \left\langle \Omega^2 \exp \left[- \left(\frac{v_j^2}{\bar{v}_j^2} + \frac{v_k^2}{\bar{v}_k^2} \right) h s^2 \right] \right\rangle \right\} \quad (2)$$

Here, $h = \frac{H_{c2,i}(T)}{H_{i0}}$ is the reduced field with the field scale $H_{i0} = \frac{8\pi T_c^2 \Phi_0}{\hbar^2 \bar{v}_j \bar{v}_k}$, i denotes the direction of the applied field, and j and k are the directions orthogonal to i . $\bar{v}_i^2 = \langle v_i^2 \rangle$, and $\langle \dots \rangle$ implies the averaging over the Fermi surface. For in-plane isotropic systems, $\bar{v}_x = \bar{v}_y$. The weight $\Omega(\mathbf{k}_F)$

accounts for possible gap anisotropy, $\Delta(\mathbf{k}_F) \propto \Omega(\mathbf{k}_F)$ and is normalized by $\langle \Omega^2 \rangle = 1$. Furthermore, we assume an in-plane gap anisotropy in the form $\Delta(\theta) = \Delta_0(1 - \alpha_6 \cos(6\theta))$ with maxima near the van Hove points as suggested by recent ARPES measurements [36, 37]. In addition to the factors describing the gap anisotropy, this model is characterized by the following parameters: r_m , the ratio of the effective masses measured along and across the saddle-shaped dispersion, $\kappa_c = K_c/p_{u0}$, the ratio of the cut off vector K_c and the separation from the van Hove point p_{u0} (see Fig. S6 [44]), t_z , a hopping integral describing dispersion in the c -direction, and E_{vH} , the location of the van Hove point below the Fermi energy at $t_z = 0$. We first consider effects of Fermi surface anisotropy only, that is, no gap anisotropy ($\alpha_6 = 0$). This version of the model describes the $H_{c2}(T)$ data well as shown in Fig. 1(d) with the parameters resulting from the simultaneous fit of the in-plane and out of plane data included in the figure. The equations underlying these fits are presented in the supplementary section [44]. We note that the relative upward curvature of $H_{c2}(T)$ for the in-plane direction is noticeably weaker than for the c -axis direction. This feature is a hallmark of the strong influence of the van Hove singularity on the upper critical field [44]. Based on this model, the upward curvature of $H_{c2}(T)$ can be characterized by the ratio of the zero-temperature and GL extrapolated values: $\frac{H_{c2,z}(0)}{H_{GL,z}} \simeq 0.295 \frac{2w_z\kappa_c}{\ln(2w_z\kappa_c)}$ [44]. Here, $w_z = \sqrt{\varepsilon_{vH}/|t_z|}$, which applies when the Fermi level crosses the van Hove energy at a certain c -axis wave vector. Due to the strong inequality $\kappa_c \gg 1$, this result implies strong upward curvature of $H_{c2}(T)$, $H_{c2,z}(0) \gg H_{GL,z}$. Using the fit parameters from Fig. 1(d), we find $H_{c2}(T)/H_{GL,z} \approx 2.35$. The reason for this curvature is the strong variation of the Fermi velocity induced by the van Hove singularities.

The effect of gap anisotropy is illustrated with simulated $H_{c2}(T)$ curves shown in Fig. S8 [44]. Interestingly, we find that the upwards curvature for the c -axis H_{c2} is suppressed due to gap anisotropy. In order to regain a good fit to the data, we need to increase the value of κ_c implying that the Fermi surface comes closer to the vHs and that anisotropy of the Fermi velocity around the Fermi surface increases. Thus, the anisotropy of the gap and of the Fermi velocity have opposing effects on the $H_{c2}(T)$ -boundary and the upwards curvature is predominantly a consequence of the large anisotropy of the Fermi velocity.

The preceding analysis aligns with recent ARPES measurements [37] that reveal superconducting gaps on three Fermi surface sheets of pristine CsV₃Sb₅. The warped cylindrical

sheet, originating from Sb orbitals centered on the Γ and A points, exhibits an isotropic gap with $\Delta \sim 0.40$ meV. Similarly, the triangular sheet centered at the K (H) points also shows an isotropic gap with $\Delta \sim 0.40$ meV. In contrast, the large hexagonal sheet around the Γ (A) points has a highly anisotropic gap, with values reaching nearly zero along the A-H direction and up to $\Delta \sim 0.65$ meV along the A-L direction. Despite this anisotropy, the average gap on this sheet appears also to be ~ 0.40 meV within the error bars. A system exhibiting superconducting gaps on multiple Fermi surface sheets that are identical behave as a single-gap superconductor. Furthermore, the upper critical field is given as an average over the Fermi surface, see Eq. (1) and (2), and therefore is not sensitive to details of the band structure but rather are determined by the average values [33]. Therefore, since the average gaps on all three Fermi surface sheets are essentially the same, we contend that the anisotropy induced by the proximity to vHS on the hexagonal sheet largely determines the observed behavior of $H_{c2}(T)$ rather than the multi-band effect.

To further investigate the effect of vHS on $H_{c2}(T)$, we employ defects created by proton irradiation to tune the electronic anisotropy through enhanced electron scattering. The temperature dependence of the resistivity of sample S1 following irradiation to a dose of 6×10^{16} p/cm² is shown in Fig. S1(e) [44]. Upon irradiation, several intriguing features are observed: (i) the residual resistivity increases significantly, from $\rho_0 \approx 1.9 \mu\Omega$ cm (at 5 K) for pristine to $\rho_0 \approx 58 \mu\Omega$ cm for the irradiated sample. (ii) T_c drops from 3.5 K (pristine) to 2.0 K (irradiated). (iii) The anomaly associated with the CDW transition becomes unobservable. (iv) The normal state MR , clearly seen for $H \parallel c$ in the pristine sample (Fig. 1(a-b)), is largely suppressed.

From the magneto-transport data presented in Figs. 2(a) and 2(b), superconducting phase diagrams are constructed for the irradiated sample as presented in Fig. 2(c). Note that the upwards curvature of $H_{c2}(T)$ seen in pristine sample turns to a conventional dirty-limit Maki-de Gennes [41-43] type variation upon irradiation. The upper critical field slopes at T_c are -1.11 T/K and -0.18 T/K for ab -plane and c -axis respectively. From the extrapolated value of the critical fields, we estimate the GL coherence length in the irradiated sample to be $\xi_c(0) \approx 4$ nm and $\xi_{ab}(0) \approx 23$ nm. With increasing disorder, both the upward curvature in $H_{c2}(T)$ and the temperature dependent superconducting anisotropy disappear as shown in Fig. 2(d), suggesting the smearing of the sharp features in the Fermi surface and of the vHS. These findings are consistent with a recent ARPES study [36] on Nb-(Ta-) substituted $\text{CsV}_{3-x}\text{Nb}_x\text{Sb}_5$ and $\text{CsV}_{3-x}\text{Ta}_x\text{Sb}_5$, which revealed identical and isotropic superconducting gaps on the three Fermi surface sheets discussed above. A

similar conclusion was reached in a study of the temperature dependence of the superconducting penetration depth of electron irradiated CsV_3Sb_5 [72].

The resistivity data described above were supplemented with magnetization and Tunnel Diode Oscillator (TDO) measurements on three crystals (S2, S3, S4) that underwent a series of consecutive irradiation runs. In the following, we highlight the observed phenomena with selected data; the complete data sets can be found in the Supplemental Materials [44]. The temperature dependence of magnetization $M(T)$ of sample S2 for various cumulative proton doses is shown in Fig. 3(a). A clear suppression of the superconducting transition is observed with increasing proton dose. Like T_c , the signature of T_{CDW} gradually weakens and eventually becomes unobservable above around $\approx 4 \times 10^{16}$ p/cm², (Fig. 3(b)).

Figure 3(c) displays the variation of T_c and T_{CDW} , normalized to their values in the pristine state, plotted as a function of proton dose. With increasing dose, both the superconducting and CDW transitions are suppressed in a nonlinear fashion, with the rate of suppression decreasing with increasing dose, such that at higher doses T_c appears to approach saturation. The simultaneous suppression of CDW and reduction of the T_c , as observed in Fig. 3(c), is unexpected for a scenario where CDW order and superconductivity compete for the same electronic density of states at the Fermi level, as seen, for instance, in cuprate and dichalcogenide superconductors [73-76]. Given that T_c and T_{CDW} are well separated in CsV_3Sb_5 , it is more likely that the observed reduction in both T_c and T_{CDW} is caused by increased scattering, rather than a direct competition between the two orders [13, 14, 77].

To quantitatively analyze the suppression of T_c with irradiation dose, we estimate a dimensionless scattering parameter [78], $g^\lambda \approx 1.05$ for $\Delta\rho_0 \approx 56.25$ ($\mu\Omega$ cm) at an irradiation dose of 6×10^{16} p/cm² [44]. While on sample S1 we have a direct measure of both $\Delta\rho_0$ and of T_c/T_{c0} , on samples S2 and S3 we obtained T_c/T_{c0} at various irradiation doses from magnetic measurements [44]. The results for both samples S2 and S3 are included in Fig. 3 (c), showing T_c suppression with increasing irradiation dose. Potential scattering in isotropic superconductors should not suppress T_c at all (Anderson theorem [79]). Thus, the observed T_c suppression with increasing disorder indicates some degree of pair-breaking scattering and/or the presence of anisotropy. However, the rate of T_c suppression with increasing disorder is much slower than that expected in the Abrikosov-Gor'kov (AG) model [78, 80] for dominant pair-breaking scattering indicating that the additional scattering due to irradiation-induced defects is predominantly not pair-breaking. In

an anisotropic s -wave superconductor, impurity scattering can average out the anisotropic gap, making the gap effectively isotropic [72, 81, 82]. Subsequently, T_c may initially drop rapidly with impurity density, but as the gap becomes more isotropic, the reduction of T_c saturates. These expectations agree with observations shown in Fig. 3(c). We also notice that the variation of T_c and T_{CDW} of CsV₃Sb₅ induced by electron irradiation [72] is similar to our proton-irradiation results.

Figure 3(d) presents the TDO data extending the susceptibility measurements down to 0.4 K, showing the temperature dependence of the normalized TDO frequency shift, $\Delta f(T)/\Delta f_0$, as highlighted in the inset. Consistent with our magnetization measurements (Fig. 3(a)), the transition temperature as observed via TDO measurement also decreases with increasing irradiation dose. By measuring $\Delta f(T)$ in various applied magnetic fields (see Fig. S5 [44]), the phase boundary $H_{c2,c}(T)$ vs T is constructed for the pristine and irradiated sample (for $H \parallel c$). The upward curvature in the $H_{c2}(T)$ gradually disappears with increasing proton dose (also see Fig. S5(g) for $H \parallel ab$), transitioning to the conventional behavior, consistent with the observations from transport measurements discussed earlier.

In summary, we investigated the temperature dependence of the upper critical field, $H_{c2}(T)$, and its anisotropy in CsV₃Sb₅ using both experimental and theoretical approaches. Our data reveal an anomalous temperature dependence of $H_{c2}(T)$, marked by a distinct upward curvature for both c -axis and in-plane magnetic fields, with zero-temperature values of ~ 1.2 T (c -axis) and ~ 6.0 T (ab -plane). Our theoretical analysis, using models for both two-band systems and a newly developed single-band incorporating vHs and gap anisotropy, reveals that the observed upper critical field behavior is predominantly driven by the anisotropy of the Fermi velocity originating from van Hove singularities rather than multi-band effects or gap anisotropy. Increased electron scattering via proton irradiation defects smears out the van Hove singularities and restores the conventional behavior. Our work underscores the critical role of ‘singularities’ in the density-of-states near the Fermi energy to the superconducting behavior.

ACKNOWLEDGMENTS

This work was supported by the U. S. Department of Energy, Office of Science, Basic Energy Sciences, Materials Sciences and Engineering Division. The proton irradiation was performed at Western Michigan University.

REFERENCES

1. D. E. Freedman, T. H. Han, A. Prodi, P. Muller, Q.-Z. Huang, Y.-S. Chen, S. M. Webb, Y. S. Lee, T. M. McQueen, and D. G. Nocera, Site specific x-ray anomalous dispersion of the geometrically frustrated kagome magnet, herbertsmithite, $\text{ZnCu}_3(\text{OH})_6\text{C}_{12}$, *J. Am. Chem. Soc.* **132**, 16185 (2010).
2. T.-H. Han, J. S. Helton, S. Chu, D. G. Nocera, J. A. Rodriguez-Rivera, C. Broholm, and Y. S. Lee, Fractionalized excitations in the spin-liquid state of a kagome-lattice antiferromagnet, *Nature* **492**, 406 (2012).
3. L. Ye, M. Kang, J. Liu, F. von Cube, C. R. Wicker, T. Suzuki, C. Jozwiak, A. Bostwick, E. Rotenberg, D. C. Bell, L. Fu, R. Comin, and J. G. Checkelsky, Massive Dirac fermions in a ferromagnetic Kagome metal, *Nature* **555**, 638 (2018).
4. S. V. Isakov, S. Wessel, R. G. Melko, K. Sengupta, and Y. B. Kim, Hard-Core Bosons on the Kagome Lattice: Valence-Bond Solids and Their Quantum Melting, *Phys. Rev. Lett.* **97**, 147202 (2006).
5. K. Nakayama, Y. Li, M. Liu, Z. Wang, T. Takahashi, Y. Yao, and T. Sato, Multiple energy scales and anisotropic energy gap in the charge-density-wave phase of the kagome superconductor CsV_3Sb_5 , *Phys. Rev. B* **104**, L161112 (2021).
6. T. Neupert, M. M. Denner, J. X. Yin, R. Thomale, and M. Z. Hasan, Charge order and superconductivity in kagome materials, *Nat. Phys.* **18**, 137 (2022).
7. B. R. Ortiz, L. C. Gomes, J. R. Morey, M. Winiarski, M. Bordelon et al., New kagome prototype materials: discovery of KV_3Sb_5 , RbV_3Sb_5 , and CsV_3Sb_5 , *Phys. Rev. Mater.* **3**, 094407 (2019).
8. B. R. Ortiz, S. M. L. Teicher, Y. Hu, J. L. Zuo, P. M. Sarte, et al., CsV_3Sb_5 : A \mathbb{Z}_2 Topological Kagome metal with a superconducting ground state, *Phys. Rev. Lett.* **125**, 247002 (2020).
9. Y. Fu, N. Zhao, Z. Chen, Q. Yin, Z. Tu, C. Gong, C. Xi, X. Zhu, Y. Sun, K. Liu, and H. Lei, Quantum transport evidence of topological band structures of Kagome superconductor CsV_3Sb_5 , *Phys. Rev. Lett.* **127**, 207002 (2021).
10. F. H. Yu, T. Wu, Z. Y. Wang, B. Lei, W. Z. Zhuo, J. J. Ying, and X. H. Chen, Concurrence of anomalous Hall effect and charge density wave in a superconducting topological kagome metal, *Phys. Rev. B* **104**, L041103 (2021).
11. S.-Y. Yang, Y. Wang, B. R. Ortiz, D. Liu, J. Gayles, et al., Giant, unconventional anomalous Hall effect in the metallic frustrated magnet candidate, KV_3Sb_5 , *Sci. Adv.* **6**, eabb6003 (2020).
12. Z. Liang, X. Hou, F. Zhang, W. Ma, P. Wu, Z. Zhang, F. Yu, J.-J. Ying, K. Jiang, L. Shan, Z. Wang, and X.-H. Chen, Three-dimensional charge density wave and surface-dependent vortex-core states in a kagome superconductor CsV_3Sb_5 , *Phys. Rev. X* **11**, 031026 (2021).
13. F. H. Yu, D. H. Ma, W. Z. Zhuo, S. Q. Liu, X. K. Wen, B. Lei, J. J. Ying, and X. H. Chen, Unusual competition of superconductivity and charge-density-wave state in a compressed topological kagome metal, *Nat. Commun.* **12**, 3645 (2021).
14. Z. Y. Zhang, Z. Chen, Y. Zhou, Y. F. Yuan, S. Y. Wang, J. Wang, H. Y. Yang, C. An, L. L. Zhang, X. D. Zhu, Y. H. Zhou, X. L. Chen, J. H. Zhou, and Z. R. Yang, Pressure-induced reemergence of superconductivity in the topological kagome metal CsV_3Sb_5 , *Phys. Rev. B* **103**, 224513 (2021).
15. J. Ge, P. Wang, Y. Xing, Q. Yin, A. Wang, J. Shen, H. Lei, Z. Wang, and J. Wang, Charge-4e and charge-6e flux quantization and higher charge superconductivity in kagome superconductor ring devices, *Phys. Rev. X* **14**, 021025 (2024).
16. S. L. Ni, S. Ma, Y. H. Zhang, J. Yuan, H. T. Yang, Z. Y. W. Lu, N. N. Wang, J. P. Sun, Z. Zhao, D. Li et al., Anisotropic superconducting properties of kagome metal CsV_3Sb_5 , *Chin. Phys. Lett.* **38**, 057403 (2021).

17. W. Duan, Z. Nie, S. Luo, F. Yu, B. R. Ortiz, L. Yin, H. Su, F. Du, A. Wang, Y. Chen, X. Lu, J. Ying, S. D. Wilson, X. Chen, Y. Song, and H. Yuan, Nodeless superconductivity in the kagome metal CsV_3Sb_5 , *Sci. China-Phys. Mech. Astron.* **64**, 107462 (2021).
18. H. D. Scammell, J. Ingham, T. Li, and O. P. Sushkov, Chiral excitonic order from twofold van Hove singularities in kagome metals, *Nat. Commun.* **14**, 605 (2023).
19. H. Tan, Y. Li, Y. Liu, D. Kaplan, Z. Wang, and B. Yan, Emergent topological quantum orbits in the charge density wave phase of kagome metal CsV_3Sb_5 , *npj Quantum Materials* **8**, 39 (2023).
20. B. R. Ortiz, S. M. L. Teicher, L. Kautzsch, P. M. Sarte, J. P. C. Ruff, R. Seshadri, and S. D. Wilson, Fermi surface mapping and the nature of charge-density-wave order in the Kagome superconductor CsV_3Sb_5 , *Phys. Rev. X* **11**, 041030 (2021).
21. M. Kang, S. Fang, J.-K. Kim, B. R. Ortiz, S. H. Ryu, J. Kim, J. Yoo, G. Sangiovanni, D. Di Sante et al, Twofold van Hove singularity and origin of charge order in topological kagome superconductor CsV_3Sb_5 , *Nat. Phys.* **18**, 301 (2022).
22. Y. Hu, X. Wu, B. R. Ortiz, S. Ju, X. Han, J. Ma, N. C. Plumb, M. Radovic, R. Thomale, S. D. Wilson, A. P. Schnyder, and M. Shi, Rich nature of van Hove singularities in kagome superconductor CsV_3Sb_5 , *Nat. Commun.* **13**, 2220 (2022).
23. H. LaBollita and A. S. Botana, Tuning the van Hove singularities in AV_3Sb_5 ($A = \text{K, Rb, Cs}$) via pressure and doping, *Phys. Rev. B* **104**, 205129 (2021).
24. Y. Luo, Y. Han, J. Liu, H. Chen, Z. Huang, L. Huai, H. Li, B. Wang, J. Shen, S. Ding et al, A unique van Hove singularity in kagome superconductor $\text{CsV}_{3-x}\text{Ta}_x\text{Sb}_5$ with enhanced superconductivity, *Nat. Commun.* **14**, 3819 (2023).
25. T. Kato, Y. Li, T. Kawakami, M. Liu, K. Nakayama, Z. Wang, A. Moriya, K. Tanaka, T. Takahashi, Y. Yao, T. Sato, Three-dimensional energy gap and origin of charge-density wave in Kagome superconductor KV_3Sb_5 , *Commun. Mater.* **3**, 30 (2022).
26. Y. Luo, S. Peng, S. M. L. Teicher, L. Huai, Y. Hu, Y. Han, B. R. Ortiz, Z. Liang, Z. Wei, J. Shen et al., Electronic states dressed by an out-of-plane supermodulation in the quasi-two-dimensional kagome superconductor CsV_3Sb_5 , *Phys. Rev. B* **105**, L241111 (2022).
27. S. D. Wilson and B. R. Ortiz, AV_3Sb_5 kagome superconductors, *Nat. Rev. Mater.* **9**, 420 (2024).
28. C. Wang, S. Liu, H. Jeon and J.-H. Cho, Origin of charge density wave in the layered kagome metal CsV_3Sb_5 , *Phys. Rev. B* **105**, 045135 (2022).
29. W.-S. Wang, Z.-Z. Li, Y.-Y. Xiang and Q. -H. Wang, Competing electronic orders on kagome at van Hove filling, *Phys. Rev. B* **87**, 115135 (2013).
30. T. Nguyen and M. Li, Electronic properties of correlated kagome metals AV_3Sb_5 ($A = \text{K, Rb, Cs}$): A perspective, *J. Appl. Phys.* **131**, 060901 (2022).
31. A. E. Koshelev, R. Chapai, D. Y. Chung, J. F. Mitchell, and U. Welp, Origin of anomalous magnetotransport in kagome superconductors AV_3Sb_5 ($A = \text{K, Rb, Cs}$), *Phys. Rev. B* **110**, 024512 (2024).
32. V. G. Kogan, R. Prozorov, and A. E. Koshelev, Temperature-dependent anisotropies of upper critical field and London penetration depth, *Phys. Rev. B* **100**, 014518 (2019).
33. M. Zehetmayer, A review of two-band superconductivity: materials and effects on the thermodynamic and reversible mixed-state properties, *Supercond. Sci. Technol.* **26**, 043001 (2013).
34. H.-S. Xu, Y.-J. Yan, R. Yin, W. Xia, S. Fang, Z. Chen, Y. Li, W. Yang, Y. Guo, and D. -L. Feng, Multiband Superconductivity with sign-preserving order parameter in Kagome superconductor CsV_3Sb_5 , *Phys. Rev. Lett.* **127**, 187004 (2021).

35. J. Liu, Q. Li, Y. Li, X. Fan, J. Li, P. Zhu, H. Deng, J.-X. Yin, H. Yang, J. Li, and H. -H. Wen, Enhancement of superconductivity and phase diagram of Ta-doped Kagome superconductor CsV₃Sb₅, *Sci. Rep.* **14**, 9580. (2024).
36. Y. Zhong, J. Liu, X. Wu, Z. Guguchia, J.-X. Yin, A. Mine, Y. Li, S. Najafzadeh, D. Das, C. Mielke III *et al.*, Nodeless electron pairing in CsV₃Sb₅-derived kagome superconductors, *Nature* **617**, 488 (2023).
37. A. Mine, Y. Zhong, J. Liu, T. Suzuki, S. Najafzadeh, T. Uchiyama, J.-X. Yin, X. Wu, X. Shi, Z. Wang, Y. Yao, and K. Okazaki, Direct observation of orbital-selective anisotropic Cooper pairing in kagome superconductor CsV₃Sb₅, arXiv:2404.18472.
38. M. J. Grant, Y. Liu, G.-H. Cao, J. A. Wilcox, Y. Guo, X. Xu, and A. Carrington, Superconducting energy gap structure of CsV₃Sb₅ from magnetic penetration depth measurements, arXiv:2411.05611 (cond-mat) (2024), <https://arxiv.org/abs/2411.05611>
39. R. Gupta, D. Das, C. H. Mielke III, Z. Guguchia, T. Shiroka, C. Baines, M. Bartkowiak, H. Luetkens, R. Khasanov, Q. Yin, Z. Tu, C. Gong, and H. Lei, Microscopic evidence for anisotropic multigap superconductivity in the CsV₃Sb₅ Kagome superconductor, *npj Quantum materials* **7**, 49 (2022).
40. Z. Shan, P. K. Biswas, S. K. Ghosh, T. Tula, A. D. Hillier *et al.*, Muon spin relaxation study of the layered Kagome superconductor CsV₃Sb₅, *Phys. Rev. Res.* **4**, 033145 (2022).
41. N. R. Werthamer, E. Helfand, and P. C. Hohenberg, Temperature and purity dependence of the superconducting critical field, H_{c2} . III. Electron spin and spin-orbit Effects, *Phys. Rev.* **147**, 295 (1966).
42. K. Maki, The magnetic properties of superconducting alloys I, *Phys.* **1**, 21 (1964).
43. P. G. de Gennes, Behavior of dirty superconductors in high magnetic fields, *Phys. Kondens. Materie.* **3**, 79 (1964).
44. See Supplemental Material for basic characterization, temperature dependence of magnetization and TDO frequency, for both pristine and irradiated samples as various proton doses, and additional details on upper critical field models for two-gap system and for open Fermi surface close to van Hove singularities.
45. R. Chapai, M. Leroux, V. Oliviero, D. Vignolles, N. Bruyant, M. P. Smylie, D. Y. Chung, M. G. Kanatzidis, W.-K. Kwok, J. F. Mitchell, U. Welp, Magnetic breakdown and topology in the Kagome superconductor CsV₃Sb₅ under high magnetic field, *Phys. Rev. Lett.* **130**, 126401 (2023).
46. K. Shrestha, R. Chapai, B. K. Pokharel, D. Miertschin, T. Nguyen *et al.*, Nontrivial Fermi surface topology of the Kagome superconductor CsV₃Sb₅ probed by de Haas-van Alphen oscillations, *Phys. Rev. B* **105**, 024508 (2022).
47. M. P. Smylie, K. Willa, H. Claus, A. Snezhko, I. Martin, W.-K. Kwok, Y. Qiu, Y. S. Hor, E. Bokari, P. Niraula, A. Kayani, V. Mishra, and U. Welp, Robust odd-parity superconductivity in the doped topological insulator Nb_xBi₂Se₃, *Phys. Rev. B* **96**, 115145 (2017).
48. Y. Wu, Q. Wang, X. Zhou, J. Wang, P. Dong, J. He, Y. Ding, B. Teng, Y. Zhang, Y. Li, *et al.*, Nonreciprocal charge transport in topological kagome superconductor CsV₃Sb₅, *npj Quantum Materials* **7**, 105 (2022).
49. X. Huang, C. Guo, C. Putzke, M. Gutierrez-Amigo, Y. Sun, M. G. Vergniory, I. Errea, D. Chen, C. Felser and P. J. Moll, Three-dimensional Fermi surfaces from charge order in layered CsV₃Sb₅, *Phys. Rev. B* **106**, 064510 (2022).
50. Y. Xiang, Q. Li, Y. Li, W. Xie, H. Yang, Z. Wang, Y. Yao, and H. -H. Wen, Twofold symmetry of *c*-axis resistivity in topological kagome superconductor CsV₃Sb₅ with in-plane rotating magnetic field, *Nat. Commun.* **12**, 6727 (2021).

51. Z. Wang, Y.-X. Jiang, J.-X. Yin, Y. Li, G.-Y. Wang, H.-L. Huang, S. Shao, J. Liu, P. Zhu, N. Shumiya, *et al.*, Electronic nature of chiral charge order in the kagome superconductor CsV₃Sb₅, *Phys. Rev. B* **104**, 075148 (2021).
52. J. Li, Q. Li, Y. Xiang, H. Yang, Z. Wang, Y. Yao, and H.-H. Wen, Local pairing versus bulk superconductivity intertwined by the charge density wave order in Cs(V_{1-x}Ta_x)₃Sb₅, *Phys. Rev. Mater.* **8**, 014801 (2024).
53. A. Gurevich, Enhancement of the upper critical field by nonmagnetic impurities in dirty two-gap superconductors, *Phys. Rev. B* **67**, 184515 (2003).
54. K. H. Müller, G. Fuchs, A. Handstein, K. Nenkov, V. N. Narozhnyi and D. Eckert, The upper critical field in superconducting MgB₂, *J. Alloys Compd*, **322**, L10 (2001).
55. L. Lyard, P. Samuely, P. Szabo, T. Klein, C. Marcenat, L. Paulius, K. H. P. Kim, C. U. Jung, H.-S. Lee, B. Kang, *et al.*, Anisotropy of the upper critical field and critical current in single crystal MgB₂, *Phys. Rev. B* **66**, 180502 (2002).
56. A. A. Golubov, and A. E. Koshelev, Upper critical field in dirty two-band superconductors: Breakdown of the anisotropic Ginzburg-Landau theory, *Phys. Rev. B* **68**, 104503 (2003).
57. D. W. Younger, and R. A. Klemm, Theory of the upper critical field in anisotropic superconductors, *Phys. Rev.* **21**, 3890 (1980).
58. P. C. Hohenberg, and N. R. Werthamer, Anisotropy and temperature dependence of the upper critical field of type-II superconductors, *Phys. Rev.* **153**, 493 (1967).
59. H. Teichler, On the theory of H_{c2} anisotropy in cubic superconductors, *Phys. Stat. Sol. (b)* **69**, 501 (1975).
60. P. Miranovic, K. Machida, V. G. Kogan, Anisotropy of the upper critical field in superconductors with anisotropic gaps: Anisotropy parameters of MgB₂, *J. Phys. Soc. Jpn.* **72**, 221 (2003).
61. J. Wang, X. Xu, N. Zhou, L. Li, X. Cao, J. Yang, Y. Li, C. Cao, J. Dai, J. Zhang, Z. Shi, B. Chen, and Z. Yang, Upward curvature of the upper critical field and the V-shaped pressure dependence of T_c in the noncentrosymmetric superconductor PbTaSe₂, *J. Supercond. Nov. Magn.* **28**, 3173 (2015).
62. M. Bristow, A. Gower, J. C. A. Prentice, M. D. Watson, Z. Zajicek, S. J. Blundell, A. A. Haghighirad, A. McCollam, and A. I. Coldea, Multiband description of the upper critical field of bulk FeSe, *Phys. Rev. B* **108**, 184507 (2023).
63. S. Khim, B. Lee, J. W. Kim, E. S. Choi, G. R. Stewart, K. H. Kim, Pauli-limiting effects in the upper critical fields of a clean LiFeAs single crystal, *Phys. Rev. B* **84**, 104502 (2011).
64. M. P. Smylie, A. E. Koshelev, K. Willa, R. Willa, W.-K. Kwok, J.-K. Bao, D. -Y. Chung, M. G. Kanatzidis, J. Singleton, F. F. Balakirev *et al.*, Anisotropic upper critical field of pristine and proton-irradiated single crystals of the magnetically ordered superconductor RbEuFe₄As₄, *Phys. Rev. B* **100**, 054507 (2019).
65. M. Bristow, W. Knafo, P. Reiss, W. Meier, P. C. Canfield, S. J. Blundell, and A. I. Coldea, Competing pairing interactions responsible for the large upper critical field in a stoichiometric iron-based superconductor CaKFe₄As₄, *Phys. Rev. B* **101**, 134502 (2020).
66. V. G. Kogan, and R. Prozorov, Orbital upper critical field and its anisotropy of clean one- and two-band superconductors, *Rep. Prog. Phys.* **75**, 114502 (2012).
67. H. Q. Yuan, J. Singleton, F. F. Balakirev, S. A. Baily, G. F. Chen, J. L. Luo, and N. L. Wang, Nearly isotropic superconductivity in (Ba,K)Fe₂As₂, *Nature* **457**, 565 (2009).
68. K. -H. Müller, G. Fuchs, A. Handstein, K. Nenkov, V. N. Narozhnyi, and D. Eckert, The upper critical field in superconducting MgB₂, *J. Alloys Compd* **322**, L11 (2001).

69. R. G. Dias and J. M. Wheatley, Superconducting upper critical field near a 2D van Hove singularity, *Solid State Commun.*, **98**, 859 (1996).
70. R. O. Zaitsev, On the effect of van Hove singularities on the critical field of type-II superconductors, *JETP Letters*, **65**, 74 (1997). (Pis'ma Zh. Eksp. Teor. Fiz. **65**, 71 (1997)).
71. R. G. Dias, Effects of van Hove singularities on the upper critical field, *J. Phys.: Condens. Matter.* **12**, 9053 (2000).
72. M. Roppongi, K. Ishihara, Y. Tanaka, K. Ogawa, K. Okada, S. Liu, K. Mukasa, Y. Mizukami, Y. Uwatoko, R. Grasset, M. Konczykowski, B. R. Ortiz, S. D. Wilson, K. Hashimoto, and T. Shibauchi, Bulk evidence of anisotropic s-wave pairing with no sign change in the kagome superconductor CsV₃Sb₅, *Nat. Commun.* **14**, 667 (2023).
73. M. Leroux, V. Mishra, J. P. C. Ruff, H. Claus, M. P. Smylie, C. Opagiste, P. Rodiere, A. Kayani, G. D. Gu, J. M. Tranquada, W. K. Kwok, Z. Islam, and U. Welp, Disorder raises the critical temperature of a cuprate superconductor, *Proc. Natl. Acad. Sci. USA* **116**, 10691 (2019).
74. F. Rullier-Albenque, H. Alloul, and R. Tourbot, Influence of pair breaking and phase fluctuations on disordered high T_c cuprate superconductors, *Phys. Rev. Lett.* **91**, 047001 (2003).
75. Y. Feng, J. Wang, R. Jaramillo, J. v. Wezel, S. Haravifard *et al.*, Order parameter fluctuations at a buried quantum critical point, *Proc. Natl. Acad. Sci. USA* **109**, 7224 (2012).
76. B. Sipos, A. F. Kusmartseva, A. Akrap, H. Berger, L. Forro *et al.*, From Mott state to superconductivity in 1T-TaS₂, *Nat. Mater.* **7**, 960(2008).
77. K. Y. Chen, N. N. Wang, Q. W. Yin, Y. H. Gu, K. Jiang, Z. J. Tu, C. S. Gong, Y. Uwatoko, J. P. Sun, H. C. Lei, J. P. Hu, and J.-G. Cheng, Double superconducting dome and triple enhancement of T_c in the Kagome superconductor CsV₃Sb₅ under high pressure, *Phys. Rev. Lett.* **126**, 247001 (2021).
78. E. I. Timmons, S. Teknowijoyo, M. Konczykowski, O. Cavani, M. A. Tanatar, S. Ghimire, K. Cho, Y. Lee, L. Ke, N. H. Jo *et al.*, Electron irradiation effects on superconductivity in PdTe₂: An application of a generalized Anderson theorem, *Phys. Rev. Res.* **2**, 023140 (2020).
79. P. W. Anderson, Theory of dirty superconductors, *J. Phys. Chem. Solids*, **11**, 26 (1959).
80. A. A. Abrikosov and L. P. Gorkov, On the theory of superconducting alloys, I. The electrodynamics of alloys at absolute zero, *Zh. Eksp. Teor. Fiz.* **35**, 1558 (1958) [*Sov. Phys. JETP* **8**, 1090 (1959)].
81. P. Hohenberg, Anisotropic superconductors with nonmagnetic impurities, *Zh. Eksp. Teor. Fiz.* **45**, 1208 (1963) (*Sov. Phys.-JETP* **18**, 834 (1964)].
82. L. A. Openov, Critical temperature of an anisotropic superconductor containing both nonmagnetic and magnetic impurities, *Phys. Rev. B* **58**, 9468 (1998).
83. J. F. Ziegler, J. P. Biersack, and M. D. Ziegler. SRIM, The Stopping and range of Ions in Matter, Ion Implantation Press (2008). Available at: www.lulu.com/content/1524197

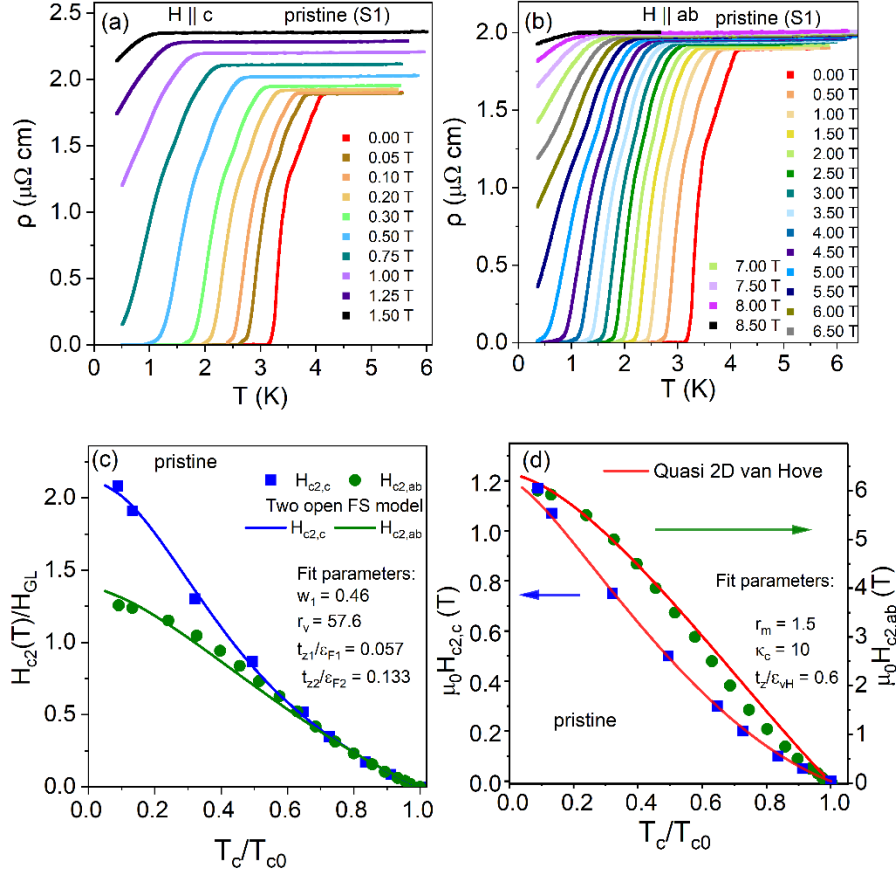


FIG. 1. Temperature dependence of the in-plane electrical resistivity $\rho(T)$ of pristine CVS (sample S1) through the superconducting transition (a) with $H \parallel c$ and (b) $H \parallel ab$ at various fields as indicated. (c) Superconducting phase diagram with field applied along c -axis (blue squares) and ab -plane (green dots), both normalized with their respective GL values of $H_{c2,c}^{GL} = 0.6$ T and $H_{c2,ab}^{GL} = 4.8$ T. The solid lines represent fits based on the model of two open Fermi surfaces (Eq. (1)). (d) H_{c2} vs T_c/T_{c0} for both orientations, fitted with the quasi-2D van Hove model (Eq. (2)).

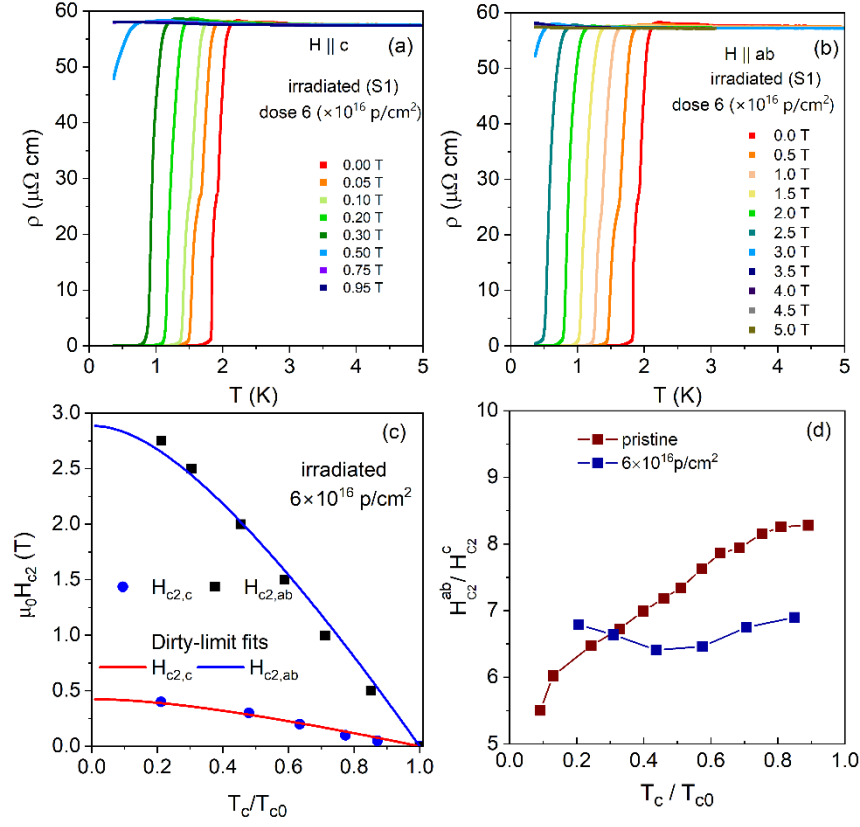


FIG. 2. The $\rho(T)$ of a crystal of CVS (sample S1) through the superconducting transition (a) with $H \parallel c$ and (b) with $H \parallel ab$ following an irradiation dose of $6 \times 10^{16} \text{ p/cm}^2$. (c) H_{c2} vs T obtained from the data in frames (a-b). Solid lines are dirty-limit fits [41]. (d) Temperature-dependent anisotropy of the pristine (red) and temperature-independent anisotropy of the irradiated sample (blue).

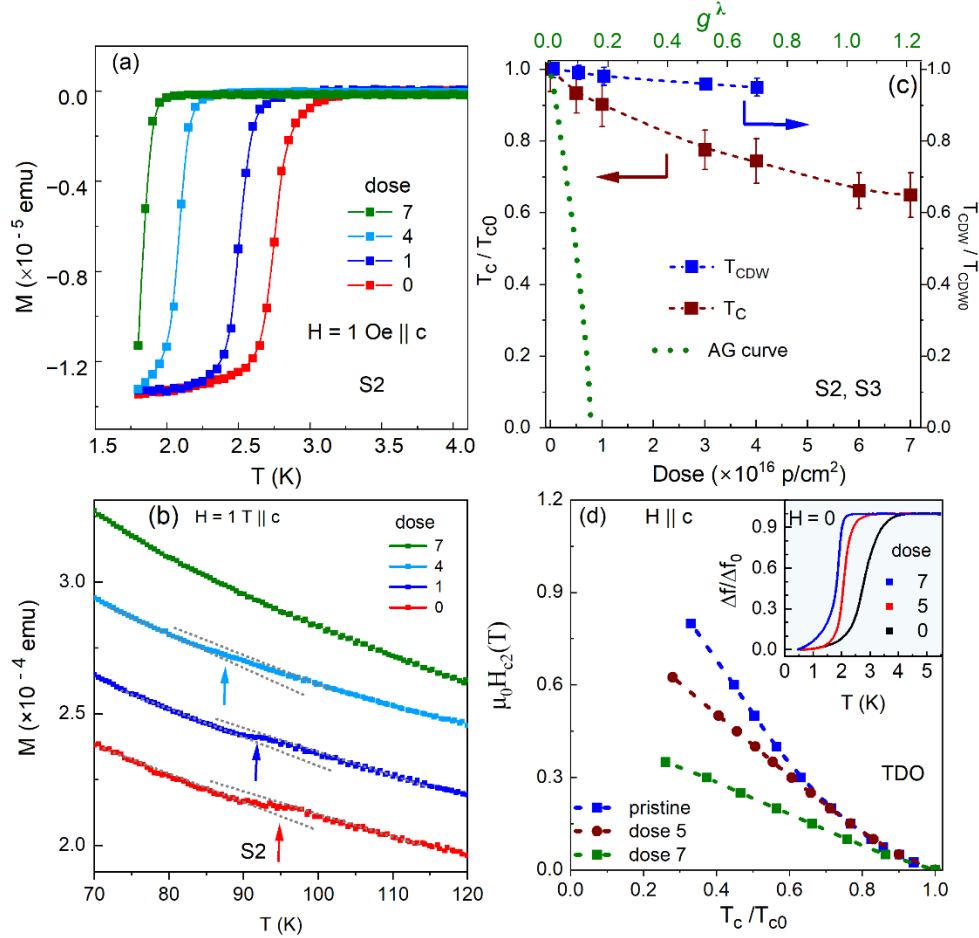


FIG. 3. (a) The superconducting transition of sample S2 as seen in the temperature dependence of the magnetic moment $M(T)$ for various proton irradiation doses. (b) $M(T)$ between 70 K and 120 K (through the CDW transition marked by the arrows). (c) Transition temperatures T_{CDW} and T_c (both normalized to the values of the pristine sample) of samples S2 and S3 vs dose. The dashed line (green) represents the suppression of T_c as expected in the AG theory for pair-breaking scattering [78]. g^λ on the top x -axis is the dimensionless scattering parameter [44]. (d) $H_{c2}(T)$ obtained from the TDO measurements for different dose levels for $H \parallel c$. Inset: Normalized TDO frequency shift vs temperature at multiple irradiation doses. The numbers specifying the irradiation dose are in units of 10^{16} p/cm 2 .

Supplemental Materials

Basic characterization

Electrical resistivity measurements of single crystalline CsV_3Sb_5 were performed in a 9-1-1 T triple-axis vector magnet inside a dilution refrigerator (Bluefors LD400) using the standard four-probe method with current applied along the ab -plane direction. The temperature dependence of the electrical resistivity, $\rho(T)$, displays two anomalies: one at $T_c \approx 3.5$ K, corresponding to superconductivity, and another at $T_{\text{CDW}} \approx 94$ K associated with the CDW transition (see FIG. S1(a)). These anomalies are also clearly seen in the temperature dependence of the magnetization $M(T)$ (shown in Fig. S1(b)) and are consistent with previous studies [8-10]. Moreover, the low residual resistivity ($\rho_0 \sim 1.2 \mu\Omega \text{ cm}$ at 5 K) and high residual resistivity ratio ($RRR \approx 52$) in $\rho(T)$ reflect the high quality of our single crystal specimens. To obtain the superconducting phase diagram, $\rho(T)$ data (in Fig. 1(a-b) in the main text) were supplemented with field dependent measurements, $\rho(H)$ (Fig.S1(c, d)), at base temperature ~ 28 mK.

Tunnel diode oscillator (TDO) measurements were performed in a custom built TDO system operating at ~ 14.5 MHz in a ^3He cryostat. Irradiation of the samples with 5-MeV protons was performed at the tandem van de Graaff accelerator at Western Michigan University. A gold foil was used to disperse the beam to ensure a uniform beam spot over the samples, and the irradiation stage was cooled to $\approx -20^\circ\text{C}$ during irradiation. For the irradiation experiment, thin samples with typical size $0.5 \times 0.5 \times 0.05 \text{ mm}^3$ were selected. The Stopping and Range of Ions in Matter (SRIM) calculations [83] for our irradiation geometry show that proton implantation in the sample is negligible. One crystal (S1) was selected for detailed magneto-transport characterization in the pristine state and after irradiation to a relatively high dose of $6 \times 10^{16} \text{ p/cm}^2$.

The temperature dependence of the resistivity $\rho(T)$ of sample S1 following irradiation to a dose of $6 \times 10^{16} \text{ p/cm}^2$ is shown in Fig. S1(e). Upon irradiation, several fascinating features are observed: (i) the residual resistivity increases significantly, from $\rho_0 \approx 1.9 \mu\Omega \text{ cm}$ (at 5 K) for pristine to $\rho_0 \approx 58 \mu\Omega \text{ cm}$ for the irradiated sample. (ii) T_c drops from 3.5 K (pristine) to 2.0 K (irradiated). (iii) The anomaly associated with the CDW transition becomes unobservable.

To analyze the suppression of T_c with irradiation dose, we estimate a dimensionless scattering parameter [78] $g^\lambda = \frac{\hbar \Delta \rho_0}{2\pi \mu_0 k_B T_{c,0} \lambda_0^2}$, yielding $g^\lambda \approx 1.05$ for $\Delta \rho_0 \approx 56.25 (\mu\Omega \text{ cm})$ at an irradiation dose of $6 \times 10^{16} \text{ p/cm}^2$ as obtained from the data in Fig. S1(c) and taking the zero-temperature penetration depth $\lambda_0 \approx 387 \text{ nm}$ [17]. As it proved challenging to maintain good electrical contacts after repeated irradiation, the systematic characterization of the dependence of T_c and T_{CDW} on irradiation dose was deduced from magnetization and susceptibility measurements on three crystals carried through a protocol of consecutive irradiations. While on sample S1 we have a direct measure of both $\Delta \rho_0$ and of $T_c/T_{c,0}$, on samples S2 and

S3 we obtained T_c/T_{c0} at various irradiation doses from magnetic measurements. Therefore, to estimate g^λ , we assume a linear relation between T_c/T_{c0} and g^λ as indicated in Fig. S1(f). The results for samples S2 and S3 are summarized in Fig. 3 (c) (main text), showing T_c suppression with increasing irradiation dose.

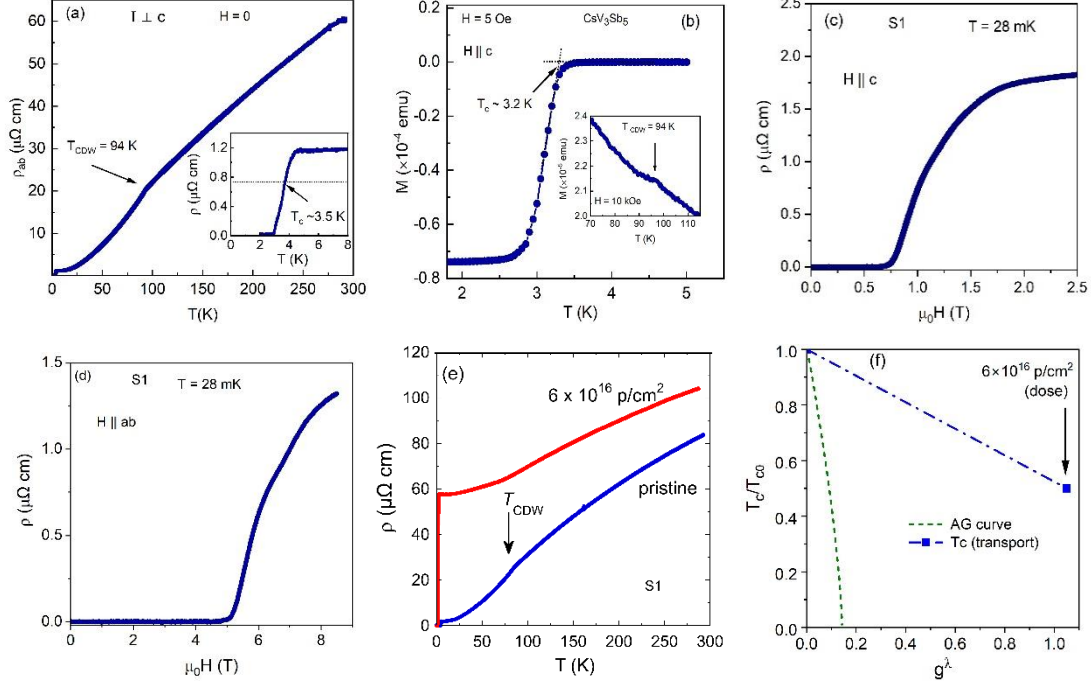


FIG. S1. (a) Temperature dependence of the in-plane electrical resistivity $\rho_{ab}(T)$ of pristine CsV_3Sb_5 between 300 K and 1.8 K displaying the CDW transition at $T_{\text{CDW}} \approx 94$ K. The inset shows the superconducting transition at $T_c \approx 3.5$ K. (b) Temperature dependence of the magnetization $M(T)$ between 1.8 K and 5 K measured by applying $H = 5$ Oe along the c axis. Inset: $M(T)$ between 70 K and 115 K measured by applying $H = 10$ kOe along the c -axis and displaying the CDW transition around $T_{\text{CDW}} \approx 94$ K. Field dependence of the in-plane electrical resistivity $\rho_{ab}(T)$ of pristine CsV_3Sb_5 under (c) $H \parallel c$, and (d) $H \parallel ab$. (e) Temperature dependence of the in-plane electrical resistivity, $\rho_{ab}(T)$, of CsV_3Sb_5 sample S1; pristine (blue) and irradiated (red). At a dose of 6×10^{16} p/cm², the CDW transition become unobservable. (f) Superconducting transition temperature (normalized to the values of the pristine sample) vs dimensionless scattering parameter (g^λ). Dashed line (green) represents the suppression of T_c expected in the AG theory [70, 80, 82].

Figure S2 (a-b) presents the temperature- and field-dependent resistivity data measured on a second single crystal (sample S5), which yields identical results to those of sample S1 (shown in Fig. 1, main text), indicating that the observed behavior is intrinsic. Specifically, for both orientations, the $H_{c2}(T)$ phase boundary displays pronounced upward curvature (see Fig. 1(c, d), main text and Fig. S2(c)). Note that while choosing a different criterion for T_c , will change the absolute values of H_{c2} , the shape of the $H_{c2}(T)$ phase boundary remains unchanged as the resistive transitions uniformly shift with the application of a magnetic field (see Fig. S2 (c)) Also, both temperature dependent and field dependent data yield the same phase boundaries.

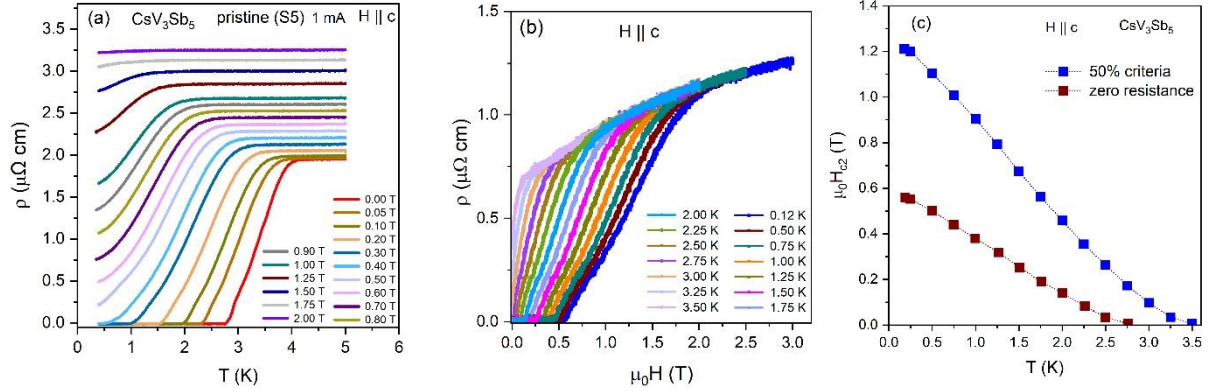


FIG. S2. (a) Temperature dependence of the electrical resistivity $\rho(T)$ of pristine CsV_3Sb_5 (sample S5) through the superconducting transition at various fields. Some structure is visible in the transition at low resistance values, well below the 50% mark. Nevertheless, the H_{c2} -data obtained on this sample are essentially identical to those on sample S1 shown in Fig. 1 of the main text, suggesting that the reported features are an intrinsic property of CsV_3Sb_5 . (b) Field dependence of the electrical resistivity $\rho(H)$ of pristine CsV_3Sb_5 (sample S5) through the superconducting transition at various temperatures. (c) Superconducting phase diagram with field applied along c -axis. The phase diagram is constructed taking two criteria, one with 50% resistance drop (blue) and other when zero resistance is reached (red).

Temperature dependent magnetization, $M(T)$ of pristine and irradiated CsV_3Sb_5

The temperature dependence of the magnetic moment $M(T)$ was measured in a superconducting quantum interference device (SQUID) magnetometer (MPMS3, Quantum Design) at various fields along the c -axis as presented in Figs. S3(a-d). The transition temperature T_c is reduced upon the application of field, consistent with a superconducting transition. Using the T_c values obtained from the onset of the transition in $M(T)$ at each field, the phase diagram of $H_{c2}(T)$ vs T is constructed, as shown in Fig. S3(e). Note that, T_c is suppressed rather abruptly until 100 Oe, and an upward curvature develops after above $T/T_c \sim 0.80$. Such characteristic features in phase diagrams have also been reported in previous experiments [16, 35] and are attributed to the multiband superconductivity [16].

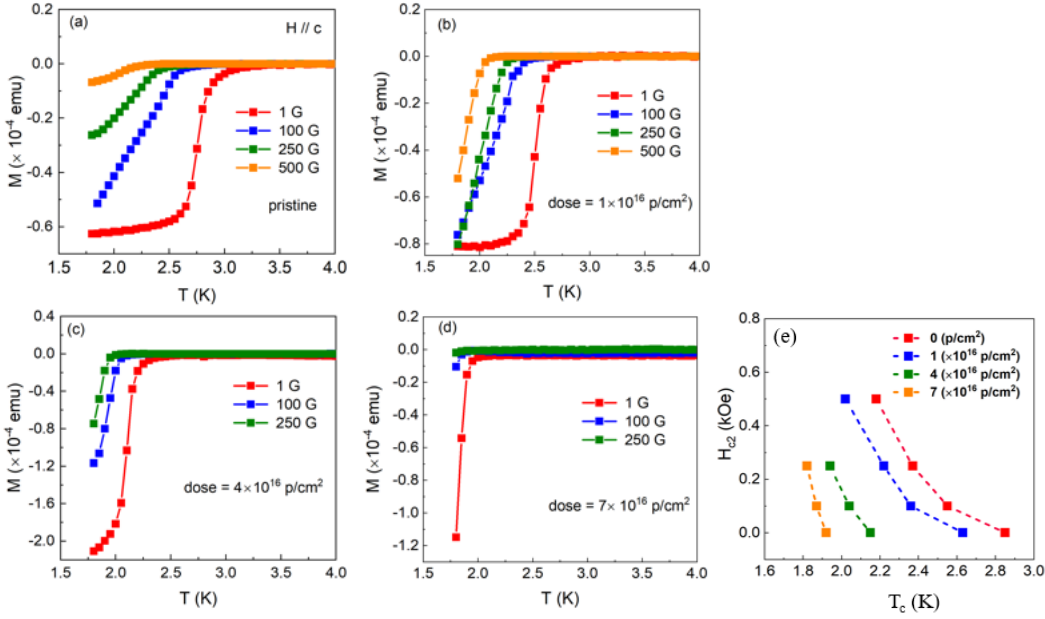


FIG. S3. (a) Temperature dependence of magnetization, $M(T)$ measured at various magnetic fields along the c -axis and as indicated with p-irradiation dose (a) pristine, (b) 1×10^{16} p/cm², (c) 4×10^{16} p/cm², (d) 7×10^{16} p/cm². (e) Superconducting phase boundary for $H \parallel c$ constructed from the data in frame a-d. Following each dose, the upwards curvature is suppressed successively consistent with the results obtained from the TDO measurement (see Fig. 3(d), main text).

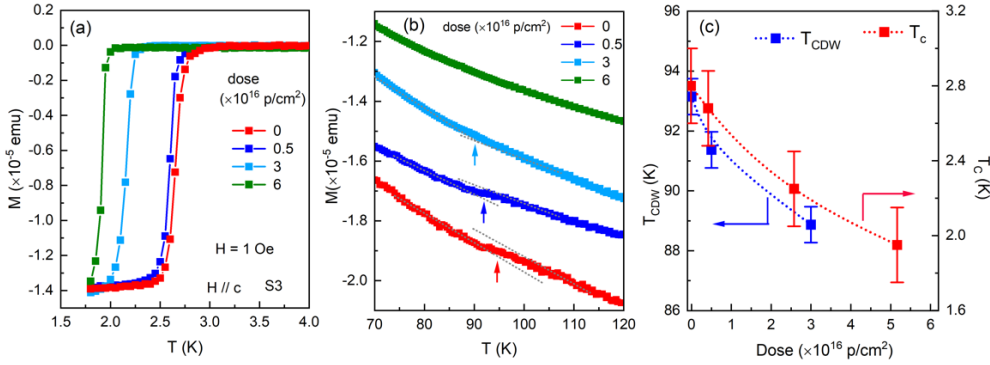


FIG. S4. Dependence of T_c and T_{CDW} of CsV₃Sb₅ sample S3 at indicated p-irradiation dose. (a) Temperature dependence of the magnetic moment, $M(T)$, at indicated doses measured by applying $H = 1$ Oe along c -axis displaying superconducting transition. (b) Temperature dependence $M(T)$ measured in a field of $H = 10$ kOe along c -axis displaying the CDW transition. (c) Transition temperatures T_{CDW} and T_c of sample S3 vs dose. These data are supplemented with the data on sample S2 in Fig. 3(c) with T_{CDW} and T_c both normalized to the values of the respective pristine sample.

Temperature dependence of the TDO frequency of the pristine and irradiated CsV₃Sb₅

The TDO technique provides highly sensitive measurements of the temperature and field dependence of the magnetic susceptibility of the sample, enabling the determination of the temperature dependence of the penetration depth and the superconducting phase diagram. Multiple CsV₃Sb₅ crystals were measured via the TDO technique. Figure S5 (a-f) shows the temperature dependence of the TDO frequency shift, $f_{\text{TDO}}(T)$, measured at various magnetic fields along the c -axis and ab plane, and at indicated p-irradiation dose.

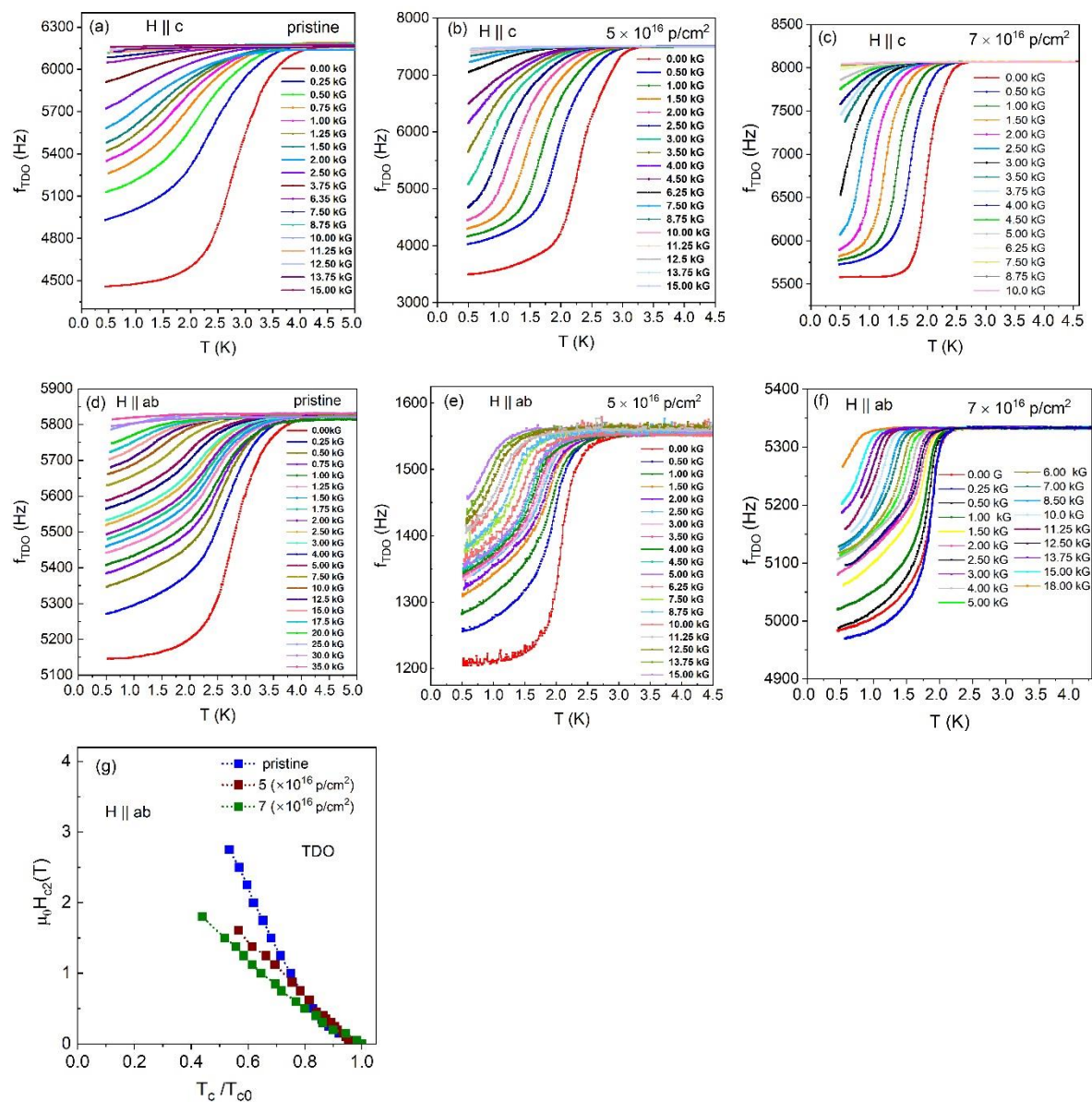


FIG. S5. (a-f) Temperature dependence of the TDO frequency measured at various magnetic fields applied along c -axis and ab plane and at indicated doses. These data are used to construct the phase diagram in Fig. 3(d) in the main text for $H \parallel c$ and Fig. S5 (g) for $H \parallel ab$.

To establish a consistent T_c criterion between measurement techniques, we use the following procedure for the TDO data. First, we find the Δf decrease from the temperature independent normal state behavior in zero applied field at the temperature equal to $T_{c,midpoint}$ from transport measurements. Here, we define this Δf as our criterion for T_c in all applied fields in TDO measurements. This approach forces T_c from both TDO and transport in zero field to be identical, gives consistent agreement of the superconducting phase boundaries determined from each technique. Measuring $\Delta f(T)$ in various applied magnetic fields (see Fig. S5 (a-f)), the phase boundary $H_{c2}(T)$ vs T is constructed for the pristine and irradiated sample for both field orientations. The upward curvature in the $H_{c2}(T)$ gradually suppresses with increasing proton dose (see Fig. 3(d), main text, for $H \parallel c$ and Fig. S5(g) for $H \parallel ab$), transitioning to the conventional behavior, consistent with the observations from transport and magnetization measurements.

Upper critical fields for two-gap layered superconductor

To model the $H_{c2}(T)$ data of CsV_3Sb_5 (see Fig. 1(c)), we consider properties of multiple-band BCS layered superconductors including gap equation and upper critical field without paramagnetic effect [41]. The general gap equation for a multiple-band BCS model is

$$\Delta_\alpha = \Lambda_{\alpha\beta} \int_0^{\omega_D} d\varepsilon \frac{\Delta_\beta}{\sqrt{\varepsilon^2 + \Delta_\beta^2}} \tanh \frac{\sqrt{\varepsilon^2 + \Delta_\beta^2}}{2T} \quad (\text{A1})$$

with the coupling-constant matrix $\Lambda_{\alpha\beta} = U_{\alpha\beta} N_\beta$, where $U_{\alpha\beta}$ are pairing interaction and N_β are partial densities of states (DOSs). In particular, for open Fermi surface and parabolic spectrum, the DOS is given by $N_\alpha = \frac{m_\alpha}{2\pi\hbar^3 s}$ where $s = 2\pi T_c \rho$ [66]. Superconducting instability develops at the eigenvector Ω_α of the matrix $\Lambda_{\alpha\beta}$ which corresponds to the largest eigenvalue λ giving the effective coupling constant, $\sum_\beta \Lambda_{\alpha\beta} \Omega_\beta = \lambda \Omega_\alpha$. This eigenvector is normalized by the condition $\sum_\alpha n_\alpha \Omega_\alpha^2 = 1$. To evaluate the temperature dependence of c -axis upper-critical field, we consider the multiple-band Eilenberger equations with finite Zeeman term and exchange field as

$$\Delta_\alpha(\mathbf{r}) = 2\pi T \sum_{\beta,\omega} \Lambda_{\alpha\beta} \langle f_\beta(\mathbf{r}, \mathbf{k}, \omega) \rangle_\beta \quad (\text{A2})$$

$$(2\omega + \mathbf{v}_\alpha \cdot \mathbf{\Pi}) f_\alpha = 2\Delta_\alpha, \quad (\text{A3})$$

where $f_\alpha(\mathbf{r}, \mathbf{k}, \omega)$ are the anomalous Green's functions, $\mathbf{\Pi} = \mathbf{\nabla} + 2\pi i\mathbf{A}/\Phi_0$, $\omega = 2\pi T \left(n + \frac{1}{2}\right)$ is the Matsubara frequency, and $\langle \dots \rangle_\beta$ implies averaging over the β Fermi sheet. A single-channel approximation corresponding to the presentation $\Delta_\alpha(\mathbf{r}) = \Psi(\mathbf{r})\Omega_\alpha$ yields

$$\Psi(\mathbf{r}) = 2\pi T \sum_{\alpha,\beta,\omega} n_\alpha \Omega_\alpha \Lambda_{\alpha\beta} \langle f_\beta(\mathbf{r}, \mathbf{k}, \omega) \rangle_\beta \quad (\text{A4})$$

$$(2\omega + \mathbf{v}_\alpha \cdot \mathbf{\Pi}) f_\alpha = 2\Psi(\mathbf{r})\Omega_\alpha \quad (\text{A5})$$

The first equation can be regularized using equation for T_c , $\Omega_\alpha = 2\pi T_c \sum_{\beta,\omega} \Lambda_{\alpha\beta} \frac{\Omega_\beta}{\omega}$, as

$$\ln \frac{T_c}{T} \Psi(\mathbf{r}) = -2\pi T \sum_{\beta, \omega} n_{\beta} \Omega_{\beta} \left\langle f_{\beta}(\mathbf{r}, \mathbf{k}, \omega) - \frac{\Psi(\mathbf{r})}{\omega} \Omega_{\beta} \right\rangle_{\beta}. \quad (\text{A6})$$

Equation (A5) can be formally solved as

$$f_{\alpha} = 2 \int_0^{\infty} d\rho \exp[-\rho(2\omega + v_{\alpha} \cdot \mathbf{\Pi})] \Psi(\mathbf{r}) \Omega_{\alpha}.$$

Substituting this solution the self-consistency equation (A6) and performing summation over ω ,

$\sum_{\omega} \exp(-2\rho\omega) = \sum_{n=0}^{\infty} \exp(-4\pi\rho T(n + 1/2)) = \frac{1}{2\sinh(2\pi\rho T)}$, we rewrite Eq. (A6) as

$$\ln \frac{T_c}{T} \Psi(\mathbf{r}) = \sum_{\alpha} w_{\alpha} \int_0^{\infty} \frac{2\pi T d\rho}{\sinh(2\pi\rho T)} (1 - \langle \exp(-\rho \mathbf{v}_{\alpha} \cdot \mathbf{\Pi}) \rangle_{\alpha}) \Psi(\mathbf{r}), \quad (\text{A7})$$

$$\text{where } w_{\alpha} = n_{\alpha} \Omega_{\alpha}^2 = \frac{n_{\alpha} \Delta_{\alpha}^2}{\sum_{\beta} n_{\beta} \Delta_{\beta}^2} \quad (\text{A8})$$

are the band widths. In particular for two bands, we can write the band weights as

$w_1 = \frac{1}{1+r_n r_{\Delta}}$ and $w_2 = \frac{r_n r_{\Delta}}{1+r_n r_{\Delta}}$, where $r_{\Delta} = \Delta_2^2/\Delta_1^2$ and $r_n = N_2/N_1$ (ratio of density of states). For quasi-

2D model, $r_n = r_m = m_2/m_1$ (ratio of effective masses). Equation (A7) has analytical solution only in few special situations such as spherical Fermi surfaces. Also, it always can be solved analytically near T_c , where it can be reduced to the Schrodinger equation for a particle in magnetic field and $\Psi(\mathbf{r})$ is given by the lowest-Landau-level wave function. In other cases, one can either solve it numerically or rely on approximations. In many cases, an approximate simpler calculation is preferable because of uncertainties of the model parameters. The simplest approximation is to project Eq. (A7) to the lowest-Landau-level wave function in the whole temperature range. For field along z axis, this approximation gives the following equation for the upper critical field

$$\ln \frac{T_c}{T} = \sum_{\alpha} w_{\alpha} \int_0^{\infty} \frac{2\pi T d\rho}{\sinh(2\pi\rho T)} \left[1 - \left\langle \exp\left(-\frac{\pi}{2} \mathbf{v}_{\alpha}^2 \frac{H\rho^2}{\Phi_0}\right) \right\rangle_{\alpha} \right]. \quad (\text{A9})$$

For numerical calculations, it is convenient to introduce the reduced variables, $t = T/T_c$, $s = 2\pi T_c \rho$,

$$\mathcal{H} = \frac{H}{H_{z0}}, H_{z0} = \frac{16\pi\Phi_0 T_c^2}{\hbar^2 v_{GL}^2}, v_{GL}^2 = \sum_{\alpha} w_{\alpha} \langle v_{\alpha}^2 \rangle_{\alpha}, \quad (\text{A10})$$

With the reduced parameters, Eq. (A9) simplifies to

$$\ln \frac{1}{t} = \sum_{\alpha} w_{\alpha} \int_0^{\infty} \frac{t ds}{\sinh(ts)} \left(1 - \left\langle \exp\left(-2\mathcal{H} \frac{v_{\alpha}^2}{v_{GL}^2} s^2\right) \right\rangle_{\alpha} \right) \quad (\text{A11})$$

One can also derive an equivalent form without 'zero over zero' behavior in the integral using $\frac{t ds}{\sinh(ts)} =$

$d \ln \tanh\left(\frac{ts}{2}\right)$ and integrating by parts

$$-\ln t = \int_0^{\infty} ds \ln \tanh\left(\frac{ts}{2}\right) \sum_{\alpha} w_{\alpha} \frac{d}{ds} \left\langle \exp\left(-2\mathcal{H} \frac{v_{\alpha}^2}{v_{GL}^2} s^2\right) \right\rangle_{\alpha}. \quad (\text{A12})$$

We now apply the above general results to the case of finite interlayer tunneling. We assume the simplest dispersion relations

$$\varepsilon(p) = \frac{p_x^2 + p_y^2}{2m} + 2t_z \cos(p_z d) - \varepsilon_F \quad (d \text{ is the } c\text{-axis lattice parameter}) \quad (\text{A13})$$

$$\text{with } 2t_z < \varepsilon_F \text{ giving } p_F(p_z) = \sqrt{2m(\varepsilon_F - 2t_z \cos(p_z d))}, v_F(p_z) = v_F \sqrt{1 - \frac{2t_z}{\varepsilon_F} \cos(p_z d)}, \quad (\text{A14})$$

$$v_x(p_z, \phi) = v_F(p_z) \cos \phi, v_z = -2t_z d \sin(p_z d) \quad (\text{A15})$$

$$\text{where } v_F = \sqrt{2\varepsilon_F/m} \text{ and } \bar{v}_x^2 = \frac{v_F^2}{2}, \bar{v}_z^2 = 2t_z^2 d^2 \quad (\text{A16})$$

$$\begin{aligned} \text{Furthermore, the average } \left\langle \exp\left(-2\mathcal{H} \frac{v^2}{v_{GL}^2} s^2\right) \right\rangle &= \int_0^\pi \frac{dq}{\pi} \exp\left[-2\mathcal{H} \frac{v_F^2}{v_{GL}^2} s^2 \left(1 - \frac{2t_z}{\varepsilon_F} \cos q\right)\right] \\ &= \exp\left(-2\mathcal{H} \frac{v_F^2}{v_{GL}^2} s^2\right) I_0\left(2\mathcal{H} \frac{v_F^2}{v_{GL}^2} \frac{2t_z}{\varepsilon_F} s^2\right), \text{ where } \int_0^\pi \frac{dx}{\pi} \exp(ax \cos x) = I_0(a). \text{ Then Eq. (A12) becomes} \end{aligned}$$

$$-\ln t = \int_0^\infty ds \ln \tanh\left(\frac{ts}{2}\right) \sum_\alpha w_\alpha \frac{d}{ds} \exp\left(-2\mathcal{H} \frac{v_{F,\alpha}^2}{v_{GL}^2} s^2\right) I_0\left(2\mathcal{H} \frac{v_{F,\alpha}^2}{v_{GL}^2} \frac{2t_{z,\alpha}}{\varepsilon_{F,\alpha}} s^2\right) \quad (\text{A17})$$

For a two-band superconductor, introducing the velocity ratio $r_v = v_{F,2}^2/v_{F,1}^2$, we can present

$$\frac{v_{F,1}^2}{v_{GL}^2} = \frac{1}{w_1 + w_2 r_v}, \quad \text{and} \quad \frac{v_{F,2}^2}{v_{GL}^2} = \frac{r_v}{w_1 + w_2 r_v},$$

where $w_2 = 1 - w_1$. For $t_{z,\alpha} \ll \varepsilon_{F,\alpha}$, the shape of the $H_{c2}(T)$ curve is determined by two parameters w_1 and r_v . Introducing the reduced function, for out-of-plane H_{c2} , one can write

$$\mathcal{G}_z(t, \tau_z, \zeta) = -\ln \frac{1}{t} + \int_0^\infty ds \ln \tanh\left(\frac{ts}{2}\right) \frac{d}{ds} [\exp(-2\zeta s^2) I_0(4\zeta \tau_z s^2)], \quad (\text{A18})$$

with $\zeta = \mathcal{H} \frac{v_\alpha^2}{v_{GL}^2}$ and $\tau_z = t_z/\varepsilon_F$. In terms of these functions, Eq. (A17) can be written as

$$\sum_\alpha w_\alpha \mathcal{G}_z\left(t, \frac{t_{z,\alpha}}{\varepsilon_{F,\alpha}}, \mathcal{H} \frac{v_\alpha^2}{v_{GL}^2}\right) = 0. \quad (\text{A19})$$

For field along ab -plane, following similar procedure for in-plane H_{c2} one can derive

$$\begin{aligned} \mathcal{G}_y(t, \tau_z, \zeta_x, \zeta_z) &= -\ln \frac{1}{t} + \int_0^\infty \frac{tds}{\sinh(ts)} \int_0^\pi \frac{dq}{\pi} \\ &\quad \{1 - \exp(-2\zeta_z \sin^2 qs^2)\} \exp[-\zeta_x (1 - 2\tau_z \cos q) s^2] I_0[\zeta_x (1 - 2\tau_z \cos q) s^2] \} \end{aligned} \quad (\text{A20})$$

with $\zeta_x = \mathcal{H} \frac{v_{F,\alpha}^2}{v_{GL}^2}$, $\zeta_z = \mathcal{H} \frac{t_{z,\alpha}^2}{\bar{t}_z^2}$, $\bar{t}_z^2 = \sum_\alpha w_\alpha t_{z,\alpha}^2$, we rewrite this equation as

$$\sum_\alpha w_\alpha \mathcal{G}_y\left(t, \frac{t_{z,\alpha}}{\varepsilon_{F,\alpha}}, \mathcal{H} \frac{v_{F,\alpha}^2}{v_{GL}^2}, \mathcal{H} \frac{t_{z,\alpha}^2}{\bar{t}_z^2}\right) = 0 \quad (\text{A21})$$

We then fit the experimental data in Fig. 1(c) (main text) using Eqs. (A18) and (A19) for $H_{c2,c}(T)$ and using Eqs. (A19) and (A20) for $H_{c2,ab}(T)$ which yields $w_1 = 0.46$, $r_v = 57.6$, $t_{z1}/\varepsilon_{F1} = 0.057$, $t_{z2}/\varepsilon_{F2} = 0.133$ and $H_{c2,c}(0) = 1.1$ T; $H_{c2,ab}(0) = 6.0$ T. The large value of the Fermi-velocity ratio squared r_v is required to reproduce the pronounced experimental upward curvature of $H_{c2,c}(T)$. The resulting fit is presented in the Fig. 1(c) of the main text.

Upper critical field for open Fermi surface close to van Hove singularities

We evaluate shapes of the temperature dependences of the upper critical field for Fermi surfaces close to van Hove singularities within quasiclassical approximation. The key feature of the electronic spectrum of the layered kagome superconductor CsV_3Sb_5 is the close proximity of several Fermi-surface sheets to van Hove singularities. Such pockets are characterized by strong variations of Fermi velocities which significantly affects the shapes of the temperature dependences of the upper critical fields. In the two-dimensional case, the influence of van Hove singularities on the upper critical field was investigated in Refs. [69-71]. To qualitatively model the shapes of the upper critical field in CsV_3Sb_5 , we use a minimum single-band model (described in Ref. [31]) and evaluate the upper critical fields for the case when the Fermi level crosses the van Hove energy. A sketch of a two-dimensional cross section of the hexagonal Fermi surface is illustrated in Fig. S6(a).

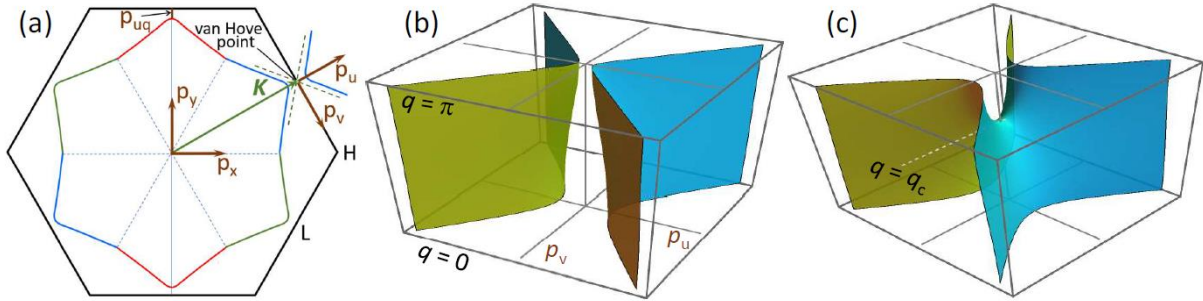


FIG. S6. (a) Finite q -cross section of the hexagonal Fermi pocket with corners close to van Hove singularities [31]. (b) Three-dimensional view of the Fermi-surface fragment near the van Hove line in the case when the Fermi level does not cross the van Hove energy. (c) Fermi-surface section in the case when the Fermi level crosses the van Hove energy at $q = q_c$.

Model for electronic spectrum

To qualitatively model the behavior of $H_{c2}(T)$ in CsV_3Sb_5 , we use a minimum single-band model with the electronic spectrum in the form: $\varepsilon(\mathbf{p}, q) = \varepsilon_{2D}(\mathbf{p}) + \varepsilon_z(q)$ where \mathbf{p} and q are in-plane and c -axis momenta, $\varepsilon_{2D}(\mathbf{p})$ is the spectrum for a single layer and $\varepsilon_z(q) = -2t_z \cos q$ is the tunneling term. The same model has been used in our previous work [31] to interpret anomalous magnetotransport in CsV_3Sb_5 . We assume that the Fermi level is close to the van Hove singularities located near six wave vectors \mathbf{K}_j with

$$K_{j,x} = K \cos\left(-\frac{\pi}{6} + \frac{\pi}{3}j\right), \quad K_{j,y} = K \sin\left(-\frac{\pi}{6} + \frac{\pi}{3}j\right), \quad (\text{B1})$$

where $j = 1, 2, \dots, 6$, $K = 2\pi/(\sqrt{3}a)$ is a half of the basic reciprocal-lattice vector for the unfolded Brillouin zone, and a is the lattice parameter (5.45 \AA for CVS). In the vicinity of these wave vectors, the spectrum has a saddle-point of the form

$$\varepsilon_{2D,j}(\mathbf{p}) = \frac{p_u^2}{2m_u} - \frac{p_v^2}{2m_v}, \quad (\text{B2})$$

where p_u and p_v are the components of the vector $\mathbf{p} - \mathbf{K}_j$ along and perpendicular to \mathbf{K}_j , respectively, see

Fig. S6(a), m_u and m_v are effective masses, and $m_v/m_u = r_m$ is their ratio. The shape of the Fermi surface is determined by equation $\varepsilon(\mathbf{p}, q) = \varepsilon_{vH}$, where ε_{vH} is the distance between the Fermi level and van Hove energy for $t_z = 0$. Depending on the relation between t_z and ε_{vH} , the Fermi level may either cross or not cross the van Hove energy as function of q . The first and second scenario is realized for $2|t_z| > \varepsilon_{vH}$ and $2|t_z| < \varepsilon_{vH}$, respectively and the corresponding Fermi surfaces are illustrated in Fig. S6(b) and (c).

c -axis upper critical field for the case of Fermi level crossing van Hove energy

Our analysis of the c -axis upper critical field is based on the quasiclassical result in Eq. (2) (see main text). In our approximate calculations, we assume the hyperbolic electronic spectrum in Eq. (B2) and will cut off the integrations along the Fermi surface at $|p_u| = K_c$, where the cutoff wave vector K_c is close to the half of the reciprocal-lattice vector K . For definiteness, we consider the case of the Fermi level crossing the van Hove energy. Since the topology of the Fermi surface changes the Fermi level crossing the van Hove energy at $q = q_c$, the averaging with respect to the c -axis wave vector has to be split into two regions

$$\langle G(v_x, v_y) \rangle = \frac{1}{\int_0^{\pi} \frac{dq}{\pi} \oint \frac{dp}{v}} \left[\int_0^{q_c} \frac{dq}{\pi} \oint \frac{dp}{v} G(v_x, v_y) + \int_{q_c}^{\pi} \frac{dq}{\pi} \oint \frac{dp}{v} G(v_x, v_y) \right]. \quad (\text{B3})$$

The Fermi surface averaging for the spectrum in Eq. (B2) can be conveniently carried out using hyperbolic parametrization [66]. For example, for $q < q_c$ the momentum components are parameterized as $p_u = p_{u0} \sqrt{1 - \vartheta_z(q)} \cosh \eta$ and $p_v = p_{v0} \sqrt{1 - \vartheta_z(q)} \sinh \eta$ with $p_{u0} = \sqrt{2m_u \varepsilon_{vH}}$ and $p_{v0} = \sqrt{2m_v \varepsilon_{vH}}$. The mean-square average of the x -component of velocity can be evaluated using the hyperbolic parametrizations as

$$\bar{v}_x^2 = \frac{v_{v0}^2 + v_{u0}^2}{4\bar{\eta}_b} \int_0^{\pi} \frac{dq}{\pi} \left(\frac{\sinh(2\eta_b)}{2} + \delta_q \eta_b \alpha_v \right) |1 - \vartheta_z(q)| \quad (\text{B4})$$

where the q -dependent parameter $\eta_b \approx \ln(2\kappa_c / \sqrt{|1 - \vartheta_z(q)|})$, $\kappa_c = K_c/p_{u0}$, $p_{u0} = \sqrt{2m_u \varepsilon_{vH}}$, $\vartheta_z(q) = \varepsilon_z(q)/\varepsilon_{vH}$, $\bar{\eta}_b = \int_0^{\pi} \frac{dq}{\pi} \eta_b(q) = \ln(2w_z \kappa_c)$, $w_z = \sqrt{\varepsilon_{vH}/|t_z|}$, $v_{u0} = \sqrt{2\varepsilon_{vH}/m_u}$, $v_{v0} = \sqrt{2\varepsilon_{vH}/m_v}$, $\alpha_v = (r_m - 1)/(r_m + 1)$, and $\delta_q = \text{sign}(q_c - q)$. In the case $\eta_b \gg 1$, we can approximately obtain

$$\bar{v}_x^2 = \frac{v_{v0}^2 + v_{u0}^2}{2r_x} \quad (\text{B5})$$

with

$$r_x \approx \frac{2}{\kappa_c^2} \ln(2w_z \kappa_c) \quad (\text{B6})$$

Here we use the analytical result for the integral

$$\int_0^{\pi} \frac{dq}{\pi} \ln |1 + a \cos q| = \ln \left(\frac{|a|}{2} \right), \text{ for } a > 1. \quad (\text{B7})$$

Using the hyperbolic parametrizations, we can approximately perform the Fermi-surface averaging in Eq.

(2) for fixed q ,

$$\begin{aligned} & \langle \exp \left[- \left(\frac{v_x^2}{\bar{v}_x^2} + \frac{v_y^2}{\bar{v}_y^2} \right) h s^2 \right] \rangle \\ &= \frac{1}{\bar{\eta}_b} \langle \int_0^{\eta_b} d\eta \exp \{ -r_x [\delta_q \alpha_v + \cosh(2\eta)] |1 - \vartheta_z(q)| h s^2 \} \rangle_q. \end{aligned}$$

This allows us to rewrite the equation for the upper critical field (Eq. (2), main text) as

$$-\ln t = \int_0^\infty \frac{t ds}{\sinh(ts)} \left\{ 1 - \frac{1}{\bar{\eta}_b} \langle \int_0^{\eta_b} d\eta \exp \{ -r_x [\delta_q \alpha_v + \cosh(2\eta)] |1 - \vartheta_z(q)| h s^2 \} \rangle_q \right\} \quad (\text{B8})$$

or

$$-\ln t = \frac{1}{\bar{\eta}_b} \int_0^\infty ds \ln \tanh \left(\frac{ts}{2} \right) \frac{d}{ds} \langle \int_0^{\eta_b} d\eta \exp \{ -r_x [\delta_q \alpha_v + \cosh(2\eta)] |1 - \vartheta_z(q)| h s^2 \} \rangle_q. \quad (\text{B9})$$

The case $2t_z < \varepsilon_{vH}$ can be treated using the same equations by setting $q_c = \pi$.

Near T_c , we can expand the right hand side of Eq. (2) (main text) with respect to h , which yields the Ginzburg-Landau linear behavior $h \simeq h_{GL}(1 - t)$ and, using the integral $\int_0^\infty \frac{s^2 ds}{\sinh s} = \frac{7\zeta(3)}{2}$, we obtain,

$h_{GL} = \frac{1}{7\zeta(3)}$. In real units, this result approximately corresponds to

$$H_{c2,z}(t) \simeq \frac{32\pi}{7\zeta(3)} \frac{T_c^2 \Phi_0}{\hbar^2 \kappa_c^2 (v_{u0}^2 + v_{v0}^2)} \ln \left(2\kappa_c \sqrt{\frac{\varepsilon_{vH}}{|t_z|}} \right) (1 - t). \quad (\text{B10})$$

Note that, contrary to the 2D case, the upper critical field linear slope dH_{c2}/dT approaches finite value for $\varepsilon_{vH} \rightarrow 0$. In the low-temperature limit, using the integral $\int_0^\infty ds \ln \left(\frac{s}{2} \right) \frac{d}{ds} \exp(-as^2) = \frac{1}{2}(\gamma_E + \ln 4a)$, where $\gamma_E = 0.5772$ is the Euler constant, Eq. (B9) can be written as

$$\gamma_E + \ln(4r_x h) + \frac{1}{\bar{\eta}_b} \langle \int_0^{\eta_b} d\eta \ln [(\delta_q \alpha_v + \cosh(2\eta))] \rangle_q + \langle \ln |1 - \vartheta_z(q)| \rangle_q = 0. \quad (\text{B11})$$

In the limit $\eta_b \gg 1$ this equation can be approximately transformed to the following form

$$\gamma_E + \ln(4r_x h) + \ln \kappa_c + \frac{1}{2} \ln \left(\frac{|t_z|}{\varepsilon_{vH}} \right) = 0, \quad (\text{B12})$$

which gives the zero-temperature upper critical field in the reduced form

$$h_{c2,z}(0) \simeq \frac{\exp(-\gamma_E)}{4} \sqrt{\frac{\varepsilon_{vH}}{|t_z|}} \frac{1}{r_x \kappa_c}. \quad (\text{B13})$$

In real units, this result corresponds to

$$H_{c2,z}(0) \simeq 4\pi \exp(-\gamma_E) \sqrt{\frac{\varepsilon_{vH}}{|t_z|}} \frac{T_c^2 \Phi_0}{\hbar^2 \kappa_c (v_{v0}^2 + v_{u0}^2)}, \quad (\text{B14})$$

The ratio of the zero-temperature and GL extrapolated values is

$$\frac{H_{c2,z}(0)}{H_{GL,z}} \simeq \frac{7\zeta(3)}{16} \exp(-\gamma_E) \sqrt{\frac{\varepsilon_{vH}}{|t_z|}} \frac{2\kappa_c}{\ln \left(2\kappa_c \sqrt{\frac{\varepsilon_{vH}}{|t_z|}} \right)}$$

Here, $\frac{7\zeta(3)}{16} \exp(-\gamma_E) = 0.295$ with $\gamma_E = 0.5772$ (the Euler constant), and for $w_z = \sqrt{\varepsilon_{vH}/|t_z|}$,

and the ratio takes the form $\frac{H_{c2,z}(0)}{H_{GL,z}} \simeq 0.295 \frac{2w_z\kappa_c}{\ln(2w_z\kappa_c)}$ which in terms of κ_c and m_u , becomes

$$\frac{H_{c2,z}(0)}{H_{GL,z}} \simeq \frac{7\zeta(3)}{8} \exp(-\gamma_E) \sqrt{\frac{K_c^2}{2m_u|t_z|}} \frac{1}{\ln\left(2\sqrt{\frac{K_c^2}{2m_u|t_z|}}\right)} \quad (\text{B15})$$

We can see that in the case of Fermi level crossing van Hove point the temperature dependence of c -axis upper critical field also has strong upward curvature due to the inequality $t_z \ll K_c^2/2m_u$.

In-plane upper critical field

For the magnetic field along the y axis, the derivation based on general quasiclassical formula in Eq. (2) (main text) gives the following presentation for the reduced in-plane upper critical field h

$$-\ln t = \int_0^\infty \frac{tds}{\sinh(ts)} \left[1 - \frac{1}{\bar{\eta}_b} \int_0^\pi \frac{dq}{\pi} \int_0^{\eta_b} d\eta \langle \exp[-(g_{x,j}(\eta) + 2\sin^2 q)hs^2] \rangle_j \right], \quad (\text{B16})$$

where $g_{x,j}(\eta)$ is the ratio v_x^2/\bar{v}_x^2 in the vicinity of the van Hove vector \mathbf{K}_j ,

$$g_{x,j}(\eta) = \begin{cases} 2r_x \frac{(\sinh \eta c_j - \sqrt{r_m} \cosh \eta s_j)^2}{1+r_m} (1 - \vartheta_z(q)), & \text{for } \vartheta_z(q) < 1 \\ 2r_x \frac{(\cosh \eta c_j + \sqrt{r_m} \sinh \eta s_j)^2}{1+r_m} (\vartheta_z(q) - 1), & \text{for } \vartheta_z(q) > 1 \end{cases}, \quad (\text{B17})$$

$c_j = \cos(\pi j/3)$, and $s_j \equiv \sin(\pi j/3)$, and $\langle \dots \rangle_j$ means averaging over the six van Hove wave vectors \mathbf{K}_j .

Near the transition temperature, the result for the linear dependence is

$$H_{c2,y}(t) = H_{GL,y}(1 - t), \quad (\text{B18})$$

$$H_{GL,y} = \frac{16\pi}{7\sqrt{2}\zeta(3)} \frac{T_c^2 \Phi_0}{\hbar \sqrt{v_{v0}^2 + v_{u0}^2} t_z d} \frac{\sqrt{\ln(2w_z\kappa_c)}}{2\kappa_c}. \quad (\text{B19})$$

This slope is also determined by the behavior of the in-plane velocities far away from the van Hove points. In the limit $\varepsilon_{vH} \rightarrow 0$ the slope diverges even slower than for the c -axis case, as the square root of the logarithm. The GL anisotropy factor for our model we can evaluate as

$$\gamma_{GL} = \frac{\sqrt{v_{v0}^2 + v_{u0}^2} \kappa_c}{2\sqrt{2}\ln(2w_z\kappa_c)t_z d/\hbar}. \quad (\text{B20})$$

Its numerical value depends on details of the in-plane velocity behavior far away from the van Hove singularities which determines the cut off wave vector K_c . In the zero-temperature limit, the reduced in-plane upper-critical field can be evaluated as

$$H_{c2,y}(0) = 2\sqrt{2}\pi \exp(-\gamma_E) \frac{T_c^2 \Phi_0}{\hbar \sqrt{v_{v0}^2 + v_{u0}^2} t_z d} \frac{\sqrt{\ln(2w_z\kappa_c)}}{2\kappa_c} \exp(-L_{av}) \quad (\text{B21})$$

with $L_{av} = \left\langle \ln \left(\frac{v_x^2}{\bar{v}_x^2} + \frac{v_z^2}{\bar{v}_z^2} \right) \right\rangle = \frac{1}{\bar{\eta}_b} \int_0^\pi \frac{dq}{\pi} \frac{1}{6} \sum_j \int_0^{\eta_b} d\eta \ln(g_{x,j}(\eta) + 2\sin^2 q)$. In the limit $\eta_b \gg 1$, we derived the following estimate $L_{av} \approx -\ln 2 + A_v 2\sqrt{2}/\bar{\eta}_b$ with $A_v = \frac{1}{6} \sum_{j=1}^6 \left| \cos \left(\frac{\pi}{3} j + \beta_v \right) \right|$ and $\beta_v = \arcsin(\sqrt{r_m}/\sqrt{1+r_m})$. The ratio of the zero-temperature and GL values for the in-plane direction can be evaluated as

$$\frac{H_{c2,y}(0)}{H_{GL,y}} = \frac{7\zeta(3)}{4} \exp(-\gamma_E - L_{av}). \quad (\text{B22})$$

This ratio is typically larger than one implying upward curvature. However, contrary to the ratio for the c -axis direction (Eq. B15), it does not contain a large parameter, meaning that for the in-plane direction upward curvature is weaker (see. FIG. 1(d) in the main text).

Representative temperature dependences of the upper critical field

Full temperature dependence of the upper critical field can be obtained by numerical solution of Eqs. (B8) and (B16). Figure S7(lower panel) shows plots of the reduced z -axis upper critical field for $k_c = 10$ and two values of t_z/ε_{vH} representing the cases of Fermi level separated from the van Hove energy ($t_z/\varepsilon_{vH} = 0.45$) and crossing the van Hove energy ($t_z/\varepsilon_{vH} = 0.6$). The latter shape approximately reproduces the observed behavior of the c -axis upper critical field in CsV₃Sb₅. We can conclude that the upward curvature of $H_{c2}(T)$ dependence for the in-plane direction is noticeably weaker than for the c -axis direction. This feature may be considered as a hallmark of strong influence of van Hove singularities on the upper critical field.

Fig. S7(top) shows plots of reduced y -axis upper critical field. The plots are made for $k_c = 10$ and two values of t_z/ε_{vH} representing the case of Fermi level separated from the van Hove energy ($t_z/\varepsilon_{vH} = 0.45$) and crossing van Hove energy ($t_z/\varepsilon_{vH} = 0.6$). The plots show upward curvature but it is somewhat weaker than the experimental results (see Fig. 1(c-d), main text).

We notice that the upwards curvature is suppressed due to gap anisotropy. To regain a good fit to the data, one needs to increase the value of κ implying that the Fermi surface comes closer to the vHs and that anisotropy of the Fermi velocity around the Fermi surface increases.

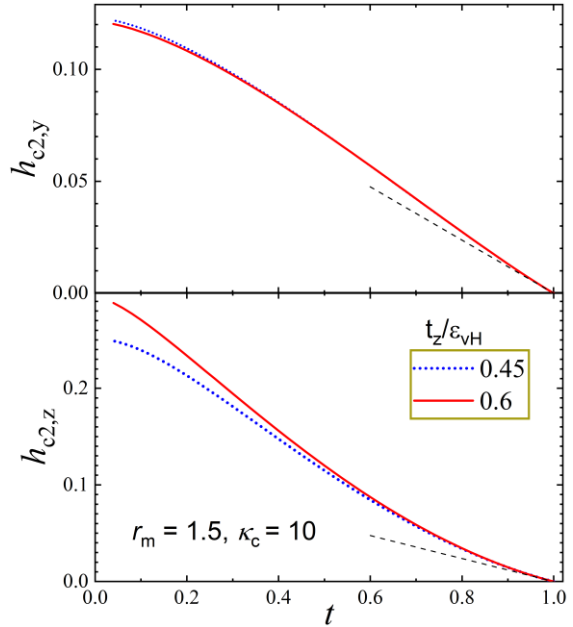


FIG. S7. Plots of reduced upper critical fields for representative parameters.

Role of gap anisotropy

We also investigated the influence of gap anisotropy on the $H_{c2}(T)$ shapes. We assume the simplest gap angular profile for a six-fold symmetric Fermi surface, $\Delta(\theta) = \Delta_0(1 - \alpha_6 \cos(6\theta))$, where θ is the polar angle. This form applies when the Fermi level does not intersect the van Hove point, $2t_z < \varepsilon_{vH}$, when the shape of Fermi surface has hexagonal cross section across the entire range of q , see Fig. S6(a). Otherwise, the polar angle does not determine the location on the single Fermi surface sheet for $q > q_c$.

For a finite gap anisotropy, we modify Eqs. (B8) and (B16) by introducing an additional factor $\Omega^2 \propto [\Delta(\theta)]^2$, normalized by the condition $\langle \Omega^2 \rangle = 1$, in which the polar angle θ has to be expressed via the hyperbolic parameter η . Since the van Hove points are located near the angles $\frac{\pi}{6} + \frac{\pi}{3}j$ in our model, for positive α_6 the gap maxima are aligned with these points. Such gap anisotropy increases the relative contribution of the Fermi-surface regions close to the van Hove singularities. As these regions have smaller Fermi velocities, this leads to a reduction of the mean-squared velocities determining the field scales H_{i0} in Eq. (2) and, consequently, to an increase of the upper critical fields at all temperatures. For the c -axis orientation, the relative increase of H_{c2} near T_c is stronger than at low temperatures, thereby reducing

the upward curvature. Figure S8 illustrates the influence of finite gap anisotropy on the shape of $H_{c2}(T)$ for two field orientations, using representative parameters. Notably, this influence is opposite for the two directions: along the c -axis, the upward curvature decreases, whereas for the in-plane direction, it slightly increases.

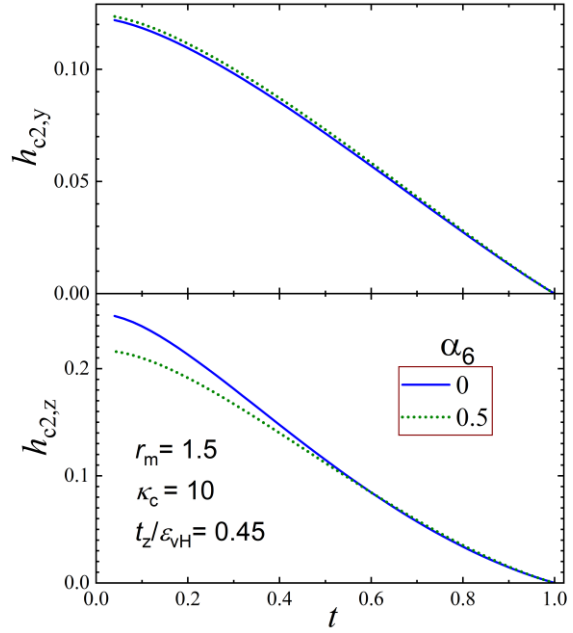


FIG. S8. The reduced upper critical fields for representative parameters illustrating the role of gap anisotropy controlled by the parameter α_6 .